Nucleus softens during herpesvirus infection

Aapo Tervonen[1,2¶], Visa Ruokolainen[1¶], Simon Leclerc[1], Katie Tieu[3], Sébastien Lyonnais[4], Henri Niskanen[5], Jian-Hua Chen[6], Alka Gupta[1], Minna U Kaikkonen[5], Carolyn A Larabell[6], Delphine Muriaux[4,7], Salla Mattola[1], Daniel E Conway[3], Teemu O Ihalainen[2], Vesa Aho[1&], Maija Vihinen-Ranta[1&].

[1]Department of Biological and Environmental Science, Nanoscience Center, University of Jyväskylä, Jyväskylä, Finland.

[2]BioMediTech, Faculty of Medicine and Health Technology, Tampere University, Tampere, Finland.

[3]Department of Biomedical Engineering, The Ohio State University, Columbus, Ohio, USA.

[4]CEMIPAI, UAR3725, CNRS, Université de Montpellier, Montpellier, France.

[5]A.I. Virtanen Institute for Molecular Sciences, University of Eastern Finland, 70211 Kuopio, Finland.

[6]Molecular Biophysics and Integrated Bioimaging Division, Lawrence Berkeley National Laboratory, Berkeley, California, USA.

[7]UMR 9004 CNRS, IRIM (Institut de Recherche en Infectiologie de Montpellier), Université de Montpellier, Montpellier, France.

*Corresponding authors:

E-mail: maija.vihinen-ranta@jyu.fi (MVR), vesa.p.aho@jyu.fi (VA)

[¶]These authors contributed equally to this work.

[&]These authors also contributed equally to this work.

Abstract

Nuclear mechanics is remodeled not only by extracellular forces but also by internal modifications, such as those induced by viral infections. During herpes simplex virus type 1 infection, the nuclear structures undergo drastic reorganization, but little is known about how nuclear mechanobiology changes as a result. We show that the nucleus softens dramatically during the infection. To understand the phenomenon, we used advanced microscopy and computational modeling. We discovered that the enlarged viral replication compartment had a low biomolecular density, partially explaining the observed nuclear softening. The mobility of the nuclear lamina decreased, which suggests increased rigidity and an inability to induce softening. However, computational modeling supported by experimental data showed that reduced outward forces, such as cytoskeletal pull and intranuclear osmotic pressure acting both on and within the nucleus, can explain the decreased nuclear stiffness. Our findings reveal that during infection, the nucleus is subject to changes in multiple mechanical forces, leading to decreased nuclear stiffness.

Author Summary

DNA viruses take over the host cell nucleus, inducing dramatic structural modifications. There is currently very little knowledge of how the progression of viral infection modifies the mechanical properties of the nucleus, which are essential for various cellular processes, including gene expression and cell migration. Here, we show that the nucleus softens when herpesvirus infection progresses. We discovered that the viral replication compartment established in the central parts of the nucleus had a low biomolecular density, which may contribute to the nuclear softening. The shape and motion of the nuclear lamina suggested that it became more rigid, indicating that another mechanism was involved in the decreased

elasticity. Our mechanical simulations and experiments showed that a reduction in outward forces, such as actin cytoskeleton pull or osmotic pressure, is the most likely factor in the nuclear softening. Our study provides new insights into the effects of DNA viruses on the mechanics of host cell nuclei, significantly expanding the knowledge of viral infection mechanobiology.

Introduction

Mechanical forces have an essential role in many cellular functions. Cells sense and react to external forces, which can lead to various responses, such as changes in gene expression and cell differentiation [1,2]. Cells also generate intracellular forces, for example, to regulate cell shape and motion [3]. The forces are transmitted via cytoskeletal filaments and can be conveyed into the nucleus and to the chromatin via transmembrane proteins in the nuclear envelope (NE). In herpes simplex virus type 1 (HSV-1)-infected cells, expansion of the viral replication compartment (VRC) and virus-induced manipulation of nuclear structure and functions most likely lead to changes in the mechanical properties of the nucleus. However, little is known about the details of these changes.

The main mechanical components of the nucleus are the NE, with its underlying nuclear lamina, and the chromatin [4,5]. Structural changes in the organization of the NE, chromatin, or both often regulate nuclear stiffness [6,7]. The nuclear lamina, a 14-nm-thick filamentous network associated with the inner nuclear membrane [8], mainly comprises intermediate filament lamins divided into A/C and B types [9]. It reinforces the NE, connects to the cytoskeleton via the linker of the nucleoskeleton and cytoskeleton (LINC) complex, and interacts with the lamina-associated domains (LADs) of the chromatin [10–12]. The nuclear

lamina, especially A-type lamins, has been shown to respond structurally to mechanical forces, and the amount of lamins is co-regulated by tissue rigidity [13,14]. Furthermore, reorganization of the lamina can change the ability of the nucleus to resist deformations and large strains [15]. The rigidity of chromatin, another regulator of nuclear stiffness, is modulated by changes in its compaction state [15–18] and by the chromatin crosslinker HP1α [19]. DNA damage and the LAD connections also contribute to the mechanical strength of the nuclei [7,20]. In addition, osmotic pressure in the nucleus has been suggested to affect its mechanical response [21]. Not only intranuclear components, but also cytoskeleton-mediated forces regulate nuclear mechanics. It has been shown that a force on the LINC complex protein nesprin-1 causes the nucleus to stiffen [22], and suppression of another LINC complex protein SUN2 results in nuclear softening [23].

Viral infections can cause drastic changes in nuclear function and structure. HSV-1 infection leads to the formation and expansion of spherical, membraneless VRCs for viral DNA replication and progeny capsid assembly [24–26], which is accompanied by reorganization of the host chromatin toward the nuclear periphery [27,28]. The VRC formation in HSV-1 and another herpesvirus, human cytomegalovirus, infection has properties similar to liquid-liquid phase separation. However, other compartmentalization mechanisms might also be included [29–31]. The substantial chromatin condensation toward the nuclear periphery regulates the diffusion of newly formed capsids through the chromatin to the NE [32–36], where the first step of nuclear egress, viral primary envelopment through the inner nuclear membrane, is assisted by the viral nuclear egress complex and the disintegration of the nuclear lamina [37–39].

96 In this study, we analyze HSV-1 infection-induced changes in the nuclear biomechanics of host
97 cells by using various experimental methods, including atomic force microscopy (AFM),
98 fluorescence lifetime imaging microscopy (FLIM), volume electron microscopy (EM), and
99 cryo-soft X-ray tomography (SXT), as well as by using computational modeling. Our data
100 show that the nuclei become softer as the infection progresses, while the nuclear structure
101 undergoes profound changes and the nuclear lamina is modified. The modeling and
102 experimental data suggest that, in addition to these changes, cytoskeletal pull on the nucleus
103 and osmotic pressure also contribute to the softening.
104

105 # Results

106 ## Nuclear stiffness decreases as the infection proceeds

107 To analyze how HSV-1 infection alters nuclear stiffness, we measured the mechanical response
108 of Vero cell nuclei to compressive force using AFM [40]. The nuclei were subjected to
109 indentation by a spherical tip of the AFM cantilever. The measurement of the bending of the
110 cantilever with a known spring constant provides the force applied to the nucleus (Figs 1A and
111 1B, see also S1 Movie), which allows quantification of its elastic modulus, i.e., nuclear stiffness
112 [41,42]. The measurements were conducted in intact cells, so although almost all the volume
113 under the tip was occupied by the nucleus, thin layers of cytoplasm remained above and below
114 the nucleus.
115
116 There was a large variation in the stiffness of noninfected cell nuclei, with values ranging from
117 200 to 3,000 Pa. Compared to noninfected cells, the mean stiffness during the infection was
118 lower at 4 hours post infection (hpi) and kept decreasing until 8 hpi, when Young's modulus

119 was only about one fourth of the noninfected cell value (Fig 1C). Finally, there was a minor
120 recovery at 10 hpi.
121
122 Our findings show that the progression of HSV-1 infection softens the nucleus. To understand
123 this phenomenon, we next studied how the infection modifies the mechanical components of
124 the nucleus, such as chromatin and the nuclear lamina.
125

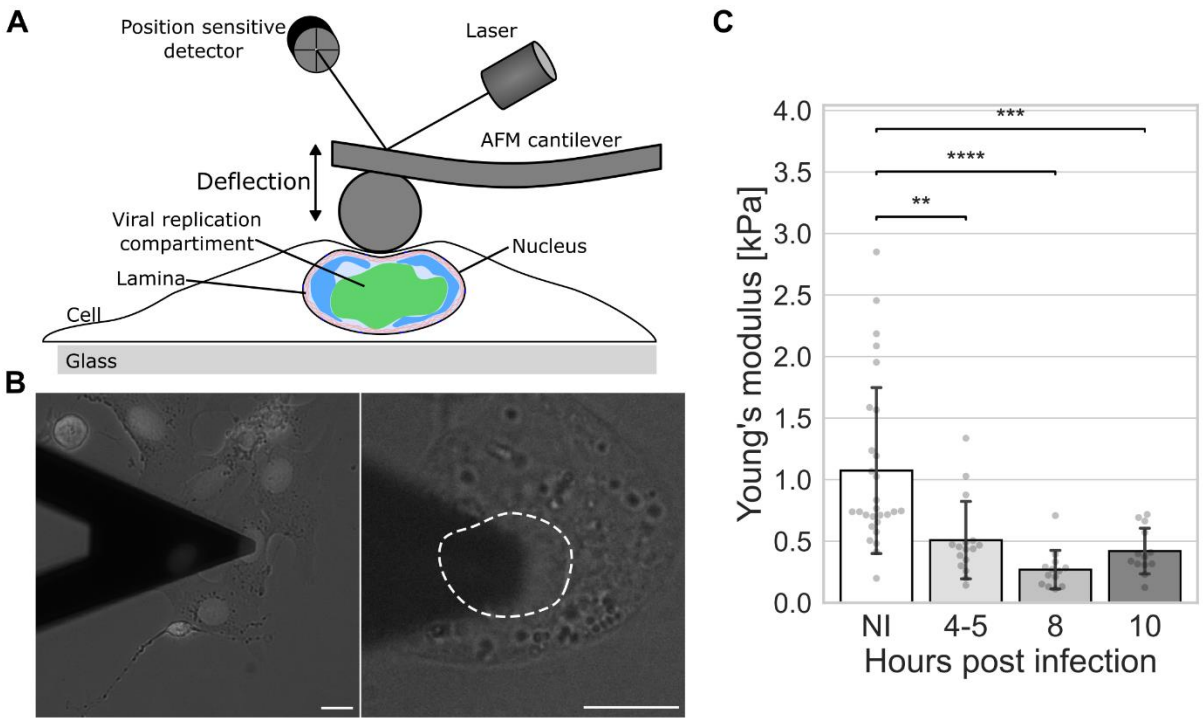

126

127 **Fig 1. Nuclear stiffness decreases in HSV-1 infection. (A)** Schematic side view of an atomic
128 force microscope (AFM) cantilever with a colloidal probe over the nuclear region of a cell. **(B)**
129 Brightfield microscopy images of an infected cell underneath the AFM cantilever at 8 hpi. The
130 nuclear periphery is demarcated by a dotted white line. Infected Vero cells were identified by
131 the presence of ICP4 by epifluorescence. See also S1 Movie. Scale bar, 10 µm. **(C)** AFM
132 analysis of nuclear stiffness performed on noninfected and HSV-1 ICP4-EYFP-infected cells
133 at 4-5, 8, and 10 hpi (n=28, 16, 13, and 13, respectively). The error bars show the standard
134 deviation. Statistical significance was determined using Tukey's test, and the significance

135 values are denoted as **** ($p < 0.0001$), *** ($p<0.001$), or ** ($p < 0.01$). Nonsignificant
136 differences ($p \geq 0.05$) are not labeled.
137

138 The molecular density of the nuclear center decreases in the 139 infection

140 In the lytic HSV-1 infection, the nuclear import of viral genomes is followed by the emergence
141 of distinct punctate VRCs at early infection (1–5 hpi) [43]. Later in infection (8–12 hpi), the
142 growth and fusion of the VRC foci result in an enlarged VRC, marginalization of host cell
143 chromatin adjacent to the nuclear envelope, and expansion of the nuclear volume [27,28,44].
144
145 SXT imaging and analysis of infected mouse embryonic fibroblast (MEF) cells showed that
146 biomolecular density, quantified by the linear absorption coefficient (LAC), in the central areas
147 of the infected cell nuclei occupied by the VRC (Figs 2A and 2B, see also S2 Movie) was lower
148 than that in the euchromatin areas of the noninfected cells (Fig 2C). The mean LAC values
149 were 0.30, 0.25, and 0.24 μm^{-1} for noninfected cells and infected cells at 4 and 8 hpi,
150 respectively. Notably, the density of the perinuclear chromatin in infected cells remained
151 similar to the density of the heterochromatin in noninfected cells, with the mean LAC value of
152 0.33 μm^{-1} for every infection time point (Fig 2D).
153
154 To further study the three-dimensional distribution and organization of chromatin in the
155 nucleoplasm of MEF cells, we used focused ion beam scanning electron microscopy (FIB-
156 SEM) and the ChromEM chromatin labeling method [45]. This approach confirmed the
157 presence of dense chromatin near the NE in infected cells at 8 hpi (Fig 2E). Notably, finger-
158 like protrusions of dense chromatin towards the center of the nucleus were less pronounced in
159 infected cells. However, small and dense chromatin aggregates were still detected in the central

area of the nucleus where the VRC and viral capsids were located (Figs 2F and 2G, see also S3 Movie). This can be cellular chromatin remaining in the VRC region or replicated viral genomes [46]. The ChromEM labeling can detect viral DNA, as shown by the intense labeling of DNA-containing capsids (S1 Fig).

In summary, the enlarged low-density region emerging during HSV-1 infection had a lower biomolecular density than euchromatin in the central parts of noninfected cell nuclei. The density decreased as the infection proceeded, which might have implications for the nuclear softness during the infection. The marginalized chromatin of the infected cell was not denser than the control cell heterochromatin.

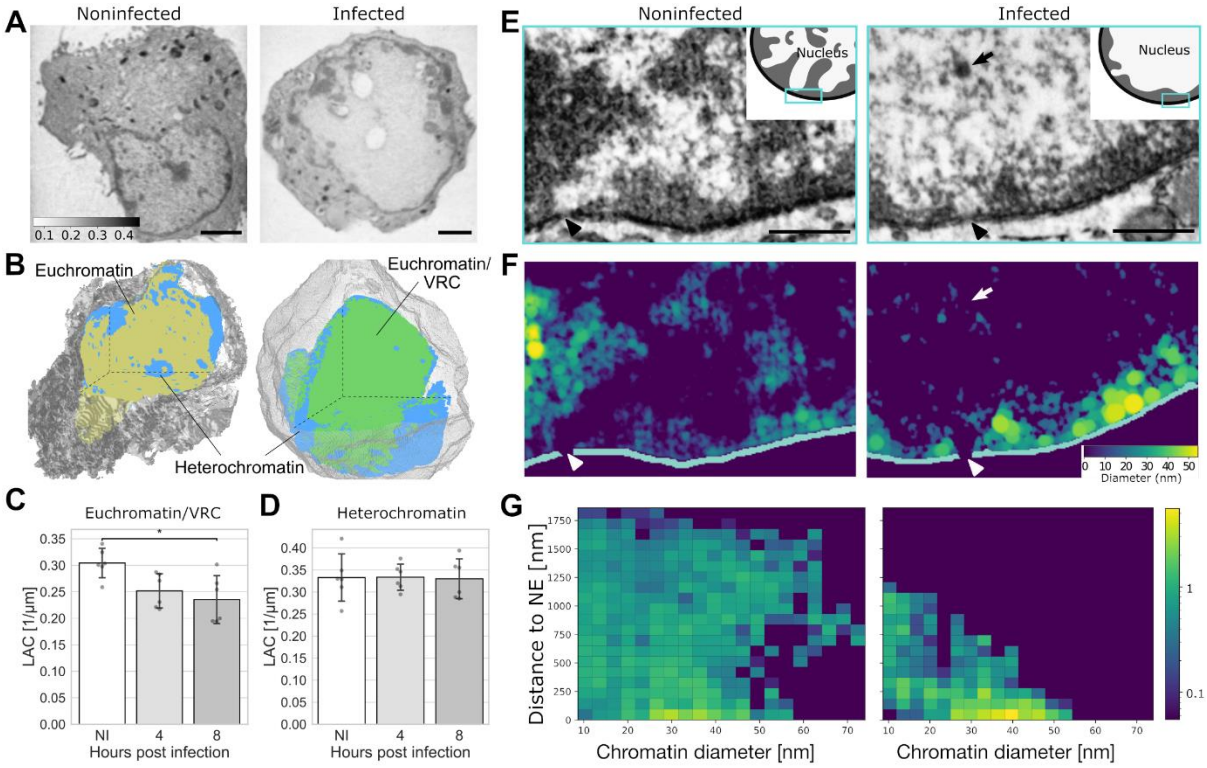

Fig 2. The enlarged viral replication compartment has a low biomolecular density. (A) Cryo-soft X-ray (SXT) tomography ortho-slices of noninfected (NI) and infected mouse embryonic fibroblast (MEF) cells at 8 hpi. Molecular densities are presented in a continuous grey scale representing linear absorption coefficient values ranging from 0.1 to 0.4 μm^{-1}

176 (calibration bar). Scale bars, 2 μm. **(B)** Cross-sections of 3D SXT reconstructions of a
177 noninfected and an infected cell. The high-density region (heterochromatin) is shown in blue,
178 the low-density region (euchromatin) in yellow, the viral replication compartment
179 (VRC/euchromatin) area in green, and the cytoplasm in grey. See also S2 Movie. Quantitative
180 analysis of linear absorption coefficient (LAC) of the **(C)** low-density and **(D)** high-density
181 region in noninfected and infected cells at 4 and 8 hpi (n=6). **(E)** Representative cross-sections
182 of focused ion beam scanning electron microscopy (FIB-SEM) images of noninfected and
183 infected MEF cells at 8 hpi. The viral capsid (arrows) and nuclear pore complexes (arrowheads)
184 are shown. Scale bars, 0.5 μm. See also S3 Movie. **(F)** Reconstruction of chromatin fiber
185 thickness and **(G)** chromatin density as a function of the distance from the nuclear envelope in
186 noninfected and infected cells. The color scale in **(F)** indicates high and low chromatin
187 thickness (yellow-blue), and in **(G)** high and low density (yellow-blue). The error bars show
188 the standard deviation. Statistical significance was determined using Tukey's test, and the
189 significance values are denoted as * ($p<0.05$). Nonsignificant differences ($p \geq 0.05$) are not
190 labeled.
191

192 The nuclear lamina motion decreases and the nuclear membrane 193 tension increases in the infection

194 Since the nuclear lamina is an essential mechanical structure for the nucleus, we used lamin
195 A/C chromobody to assess differences in the nuclear lamina shape and motion in noninfected
196 and infected living Vero cells [47]. We hypothesized that the mechanical stiffness of the
197 nuclear lamina is linked to its shape and mobility, and that an increase (or decrease) in internal
198 pressure would cause the nucleus to bulge (or wrinkle).
199

200 To analyze the lamina shape, it was segmented, skeletonized, and discretized. Local regions of
201 positive and negative curvature with respect to the nuclear interior were then quantified (Fig
202 3A). The proportion of negative curvature regions was smallest at 8 hpi, but the change was
203 not statistically significant (Fig 3B). Next, the extent of lamina fluctuations was analyzed by
204 taking the maximum intensity projection of the segmented and skeletonized lamina over the
205 time series and calculating its area (Fig 3C). The motion of the nuclear lamina, quantified as
206 the area covered by the lamina skeleton during the time series and normalized by the length of
207 the lamina, was significantly smaller at 8 hpi than in noninfected cells (Fig 3D). This shows
208 that the motion of the lamina decreases in infection, indicating higher tension or reduced
209 mechanical dynamics. Finally, nuclear membrane tension was measured by the ER Flipper-TR
210 probe and FLIM [48]. Changes in the fluorescence lifetime indicated increased tension in the
211 NE at 12 hpi compared to noninfected cells, although at 8 hpi the membrane tension was similar
212 to that in the noninfected cells (Figs 3E and 3F).
213
214 Finally, we analyzed the significance of lamins in the infection-induced nuclear growth in Vero
215 cells by using overexpression of A-type lamins and the presence of truncated and farnesylated
216 lamin A protein, progerin [49]. Confocal microscopy showed that the progression of infection
217 and overexpression of lamin A/C increased nuclear volume, whereas the presence of progerin
218 reduced it (S2 Fig).
219

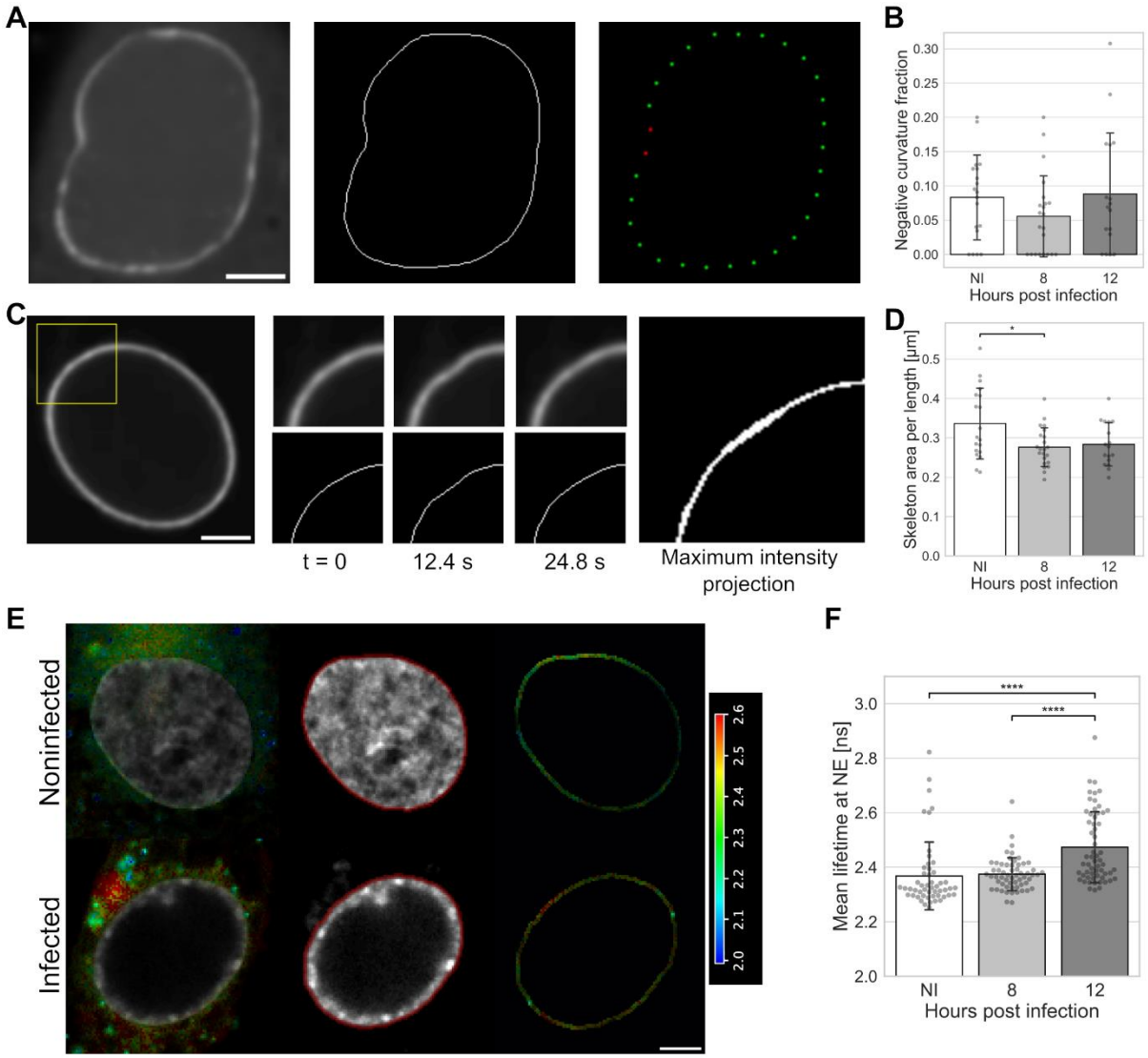

Fig 3. The motion of the nuclear lamina decreases in infection. (A) Nuclear lamina labeled by lamin A chromobody, skeletonization of the lamina, and discretized lamina points showing regions of positive (green) and negative curvature (red) in infected Vero cells at 8 hpi. **(B)** The fraction of negative curvature points for noninfected cells and cells imaged 8 and 12 hpi (n=19, 22, and 17, respectively). **(C)** A zoom-in of the nuclear lamina, showing its motion and maximum intensity projection of the skeleton during 24.8 s. Scale bars, 5 µm. **(D)** Nuclear lamina mobility, measured as the area covered by the skeleton during one minute for noninfected cells and cells imaged 8 and 12 hpi (n=19, 22, and 17, respectively). **(E)** Nuclear envelope (NE) tension analysis by fluorescence lifetime imaging microscopy (FLIM) of noninfected and HSV-1 17+ wild-type virus-infected Vero cells at 12 hpi using fluorescence

231 lifetime-reporting membrane tension probe ER Flipper-TR. A fast FLIM image presented in a
232 pseudocolor scale representing average photon arrival times in each pixel, ranging from 2.0 to
233 2.6 ns (calibration bar). Representative cells with average lifetime distribution, segmented NE
234 (red) around the Hoechst signal (grey), and average lifetime at the NE region are shown. Scale
235 bar, 10 μm. **(F)** The longer lifetime component of the ER Flipper probe, responsive to the
236 membrane tension, in noninfected and infected cells at 8 and 12 hpi (n=51, 58, and 59,
237 respectively). The error bars show the standard deviation. Statistical significance was
238 determined using Tukey's test, and the significance values are denoted as * ($p<0.05$) or ****
239 ($p<0.0001$). Nonsignificant differences ($p \geq 0.05$) are not labeled.
240

241 # SUN2 expression decreases in infection

242 The nuclear lamina is one of the significant determinants of the mechanical behavior of the
243 nucleus. Thus, to explore the transcriptional activity of lamina-associated proteins during
244 infection, we performed global run-on sequencing (GRO-Seq) in Vero cells. The gene ontology
245 analysis (GO) of GRO-Seq data according to the PANTHER classification system for the GO
246 biological process (http://www.pantherdb.org) identified three main categories: protein
247 localization to the NE (GO:0090435), nuclear migration (GO:0007097), and NE organization
248 (GO:0006998) (Figs 4A and 4B, see also S1 Table).
249

250 At 4 hpi, the genes encoding lamins A/C and B2 were upregulated compared to noninfected
251 control cells, whereas at 8 hpi, the genes encoding lamins B1 and B2 were downregulated.
252 Notably, transcription of SUN2, one of the essential proteins of the LINC complex and the key
253 regulator of nucleus-cytoskeleton connections [50], was strongly downregulated at 8 hpi. The
254 zinc metallopeptidase STE24 (ZMPSTE24), a protein needed during the preprocessing of
255 lamin A [51], was upregulated at 4 and 8 hpi. This protein has a potent antiviral activity,

256 inhibiting the replication of many enveloped DNA and RNA viruses [52,53]. At 4 and 8 hpi,
257 torsin-1A-interacting protein 1 (TOR1AIP1, also known as LAP1), a protein involved in the
258 connection between the nuclear membrane and the nuclear lamina [54,55], was upregulated.
259 The downregulation of SUN2 at 8 hpi could decrease overall interactions between SUN2 and
260 LINC complex components, including nesprin family proteins encoded by SYNE 1–4 genes
261 [56]. The clustering of genes (https://string-db.org/) (Fig 4C and S1 Table) confirmed an
262 interaction between SUN2 and lamin A/C, which further interacted with lamin B2. In addition,
263 lamin A/C interacted with the upregulated TOR1AIP1.
264
265 Consistent with the GRO-seq data, western blot analysis showed that HSV-1 infection
266 downregulated SUN2 expression at 8 hpi and, especially, at 12 hpi compared to noninfected
267 cells. Our results are consistent with previous studies indicating a decrease in SUN2 protein
268 levels at late stages of HSV-1 infection [57]. Protein expression levels of lamin A at 8 and 12
269 hpi were not significantly different from those of noninfected cells. The infection led to a slight
270 downregulation of lamin B2 expression at 8 and 12 hpi, although this was not statistically
271 significant (Figs 4D and 4E, see also S3 Fig). Altogether, our findings show that progression
272 of infection led to downregulation of the key regulator of cytoskeleton–nucleus force
273 transmission, the LINC complex protein SUN2, but did not significantly alter the expression
274 of nuclear lamina proteins.

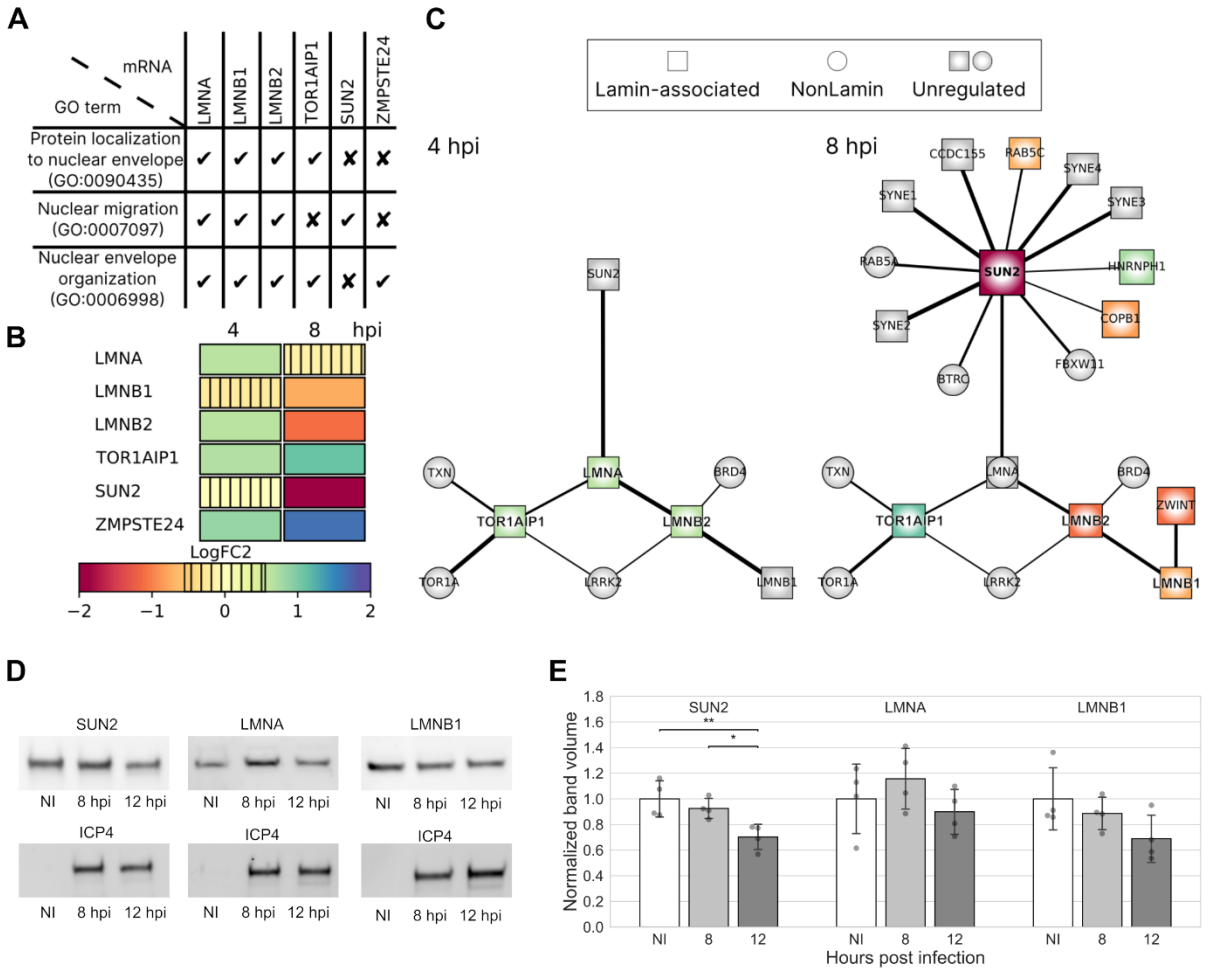

Fig 4. The amount of SUN2 decreases in infection. Global run-on sequencing (GRO-seq) analysis of nascent RNA levels of nuclear lamins and lamin-associated proteins in infected Vero cells at 4 and 8 hpi. **(A)** GO term classification for lamin-associated processes and **(B)** regulation of proteins. The color scale indicates upregulation (green-blue), downregulation (orange-red), or low change of gene transcription (vertical stripes) compared to noninfected control cells. **(C)** The genes encoding for lamins and lamin-associated proteins (square nodes) and cellular interactor proteins not associated with lamins (circular nodes) are shown. The upregulated (green-blue) or downregulated (red-orange) transcripts in response to the infection are visible together with unregulated interacting transcripts (grey). The node size correlates with the logarithmic fold change (logFC) of regulation, and the thickness of black lines between the nodes is proportional to the interaction in the STRING database (https://string-db.org/). **(D)** Representative western blots showing the expression of SUN2, lamin A, and lamin B in

288 noninfected and infected cells at 8 and 12 hpi. Viral ICP4 was used as an infection marker. **(E)**
289 Quantitative analysis of western blots (n = 4). The error bars show the standard deviation.
290 Statistical significance was determined using Tukey's test, and the significance values are
291 denoted as ** ($p<0.01$) or * ($p<0.05$). Nonsignificant differences ($p \geq 0.05$) are not labeled.
292

293 Computational modeling of nuclear mechanics

294 Our experimental data indicated that the nuclear lamina becomes less mobile, which suggests
295 that the NE becomes stiffer during the infection. However, AFM indentation measurements
296 suggested that nuclear stiffness decreases during the infection. To understand this seeming
297 contradiction, we built a computational model of the nucleus to simulate scenarios that could
298 lead to the observed changes. The main model assumptions are: (1) the mechanical properties
299 of the nucleus are governed by the nuclear envelope, including nuclear lamina, chromatin, and
300 outward forces, representing actin cytoskeleton pull on the nucleus and osmotic pressure
301 difference; (2) viscous changes in the nuclear structures occur on a time scale too slow to affect
302 the fast AFM measurement; and (3) the VRC is soft and does not interfere with the AFM
303 measurement.
304

305 The model consisted of two components that determine the main mechanical properties of the
306 nucleus: the NE, which is considered to include the nuclear lamina, and chromatin. The NE
307 was modeled as a thin 3D triangulated shell, and 46 separate polymers inside the shell
308 represented the chromatin. Furthermore, connections between the two, the LADs, and transient
309 cross-links within the chromatin were included in the model. Additionally, an outward force
310 was included to represent the combined effects of outward cytoskeletal forces on the NE and
311 osmotic pressure. The NE in the model includes all the mechanics related to changes in nuclear
312 surface area, while the chromatin and outward forces together describe the mechanics

313 associated with nuclear volume. Initial simulations indicated that both the nuclear area- and
314 volume-related components contribute to the total nuclear stiffness. Finally, to model the VRC,
315 another shell, similar to the NE, was added inside the nucleus and grown to an appropriate size
316 to marginalize the chromatin towards the periphery (Fig 5A and S4 Movie). Model parameters
317 for the noninfected nucleus were taken from the literature or fitted by replicating the AFM
318 experiments (S5 Movie). The developed model has certain limitations. Combining the
319 cytoskeletal pull and osmotic pressure into the outward forces reduces the ability of the model
320 to predict the specific cause of the decreased outward force. Additionally, the model does not
321 distinguish between heterochromatin and euchromatin, so it cannot describe the mechanical
322 differences between them. However, adding these features would increase the number of
323 unknown parameters that need to be estimated, thereby reducing the usability of the model.
324
325 To study nuclear mechanics during HSV-1 infection, various model parameters were iteratively
326 adjusted to observe their impact on simulated AFM results. Based on the observed low
327 molecular density (Figs 1A-1C), we hypothesized that the VRC is very soft and therefore
328 disregarded its mechanical role in the infected cell AFM simulations. Additionally, we
329 postulated that most of the changes seen in Young's modulus were due to the morphological
330 and structural alterations of the nucleus rather than the cytoplasm. First, we examined the
331 effects of changes in nuclear volume and height on the simulated AFM results while keeping
332 everything else constant (Fig 5B, see also S2 Fig). While there was no change in the simulated
333 Young's moduli between the noninfected and 8 hpi similar-sized nuclei, the increase in the
334 nuclear size at 12 hpi led to a significant increase in the simulated stiffness compared to the
335 noninfected nuclei. Next, we simulated the effect of chromatin marginalization on the
336 simulated Young's moduli and found no significant change (Fig 5C). Finally, we investigated
337 the importance of lamina-chromatin tethering by simulating the 8 hpi nuclei with and without

338 LADs. We found that the omission of LADs significantly reduced Young's modulus (Fig 5D).
339 However, this decrease in stiffness was relatively minor compared to the experimentally
340 observed change between noninfected and 8 hpi nuclei. Therefore, since these changes in the
341 nucleus could not explain the experimentally observed reduction in nuclear stiffness, other
342 mechanical changes must occur during HSV-1 infection.
343
344 To understand the changes in nuclear mechanics that could reduce nuclear stiffness, we focused
345 on two key changes: decreased outward force and lamina disintegration (Fig 5E). The first
346 change involves a decrease in cytoskeletal force on the nucleus via the LINC complexes or an
347 osmotic pressure difference between the cytoplasm and the nucleus. The second change, lamina
348 disintegration, a phenomenon observed during HSV-1 infection, was implemented by reducing
349 the mechanical strength of a given percentage of connections in the lamina, without altering
350 the number of LADs. Decrease in the outward forces had the most significant effect, as shown
351 by the reduction of the simulated Young's moduli (Fig 5F). Lamina disintegration was
352 generally insignificant when the outward forces were high, but became more important at lower
353 outward force strengths. Thus, our computational data suggested that outward forces, including
354 cytoskeletal forces and osmotic pressure, had the most prominent effect on nuclear stiffness.
355
356 Next, we used the model to study whether the experimentally observed increase in NE
357 membrane tension during the infection can co-occur with decreased outward forces and
358 disintegration of the lamin network. We found that tension in the nuclear membrane is affected
359 by both lamina disintegration and the decrease in outward forces (Fig 5G). Lamina
360 disintegration increased nuclear membrane tension, whereas a reduction in outward forces
361 decreased it. The increase in membrane tension during lamina disintegration can be explained
362 by a larger share of the outward forces acting on the membrane rather than on the lamina.

Importantly, these results show that the combined effects of lamina disintegration and reduced outward forces can lead to a constant or increased NE membrane tension during infection. Furthermore, we compared the distribution of lamina tension in the NE as the lamina was disintegrated (Figs 5H and 5I). There were more local high-tension spots on the top surface of the nucleus as the lamina disintegrated, which led to an overall increase in the nuclear lamina tension. In all cases, the tension was higher on the sides of the nucleus (Fig 5H), which is explained by the absence of an actin cap to counteract the outward nuclear forces in these regions. Taken together, the simulation results indicate that the decrease in nuclear stiffness during HSV-1 infection is a consequence of reduced cytoskeletal forces and osmotic pressure, rather than of lamina disintegration. Also, reduced nuclear stiffness can coincide with increases in nuclear membrane and local lamina tension. Lastly, based on our assumptions and simulations, chromatin marginalization did not affect the nuclear stiffness during the infection.

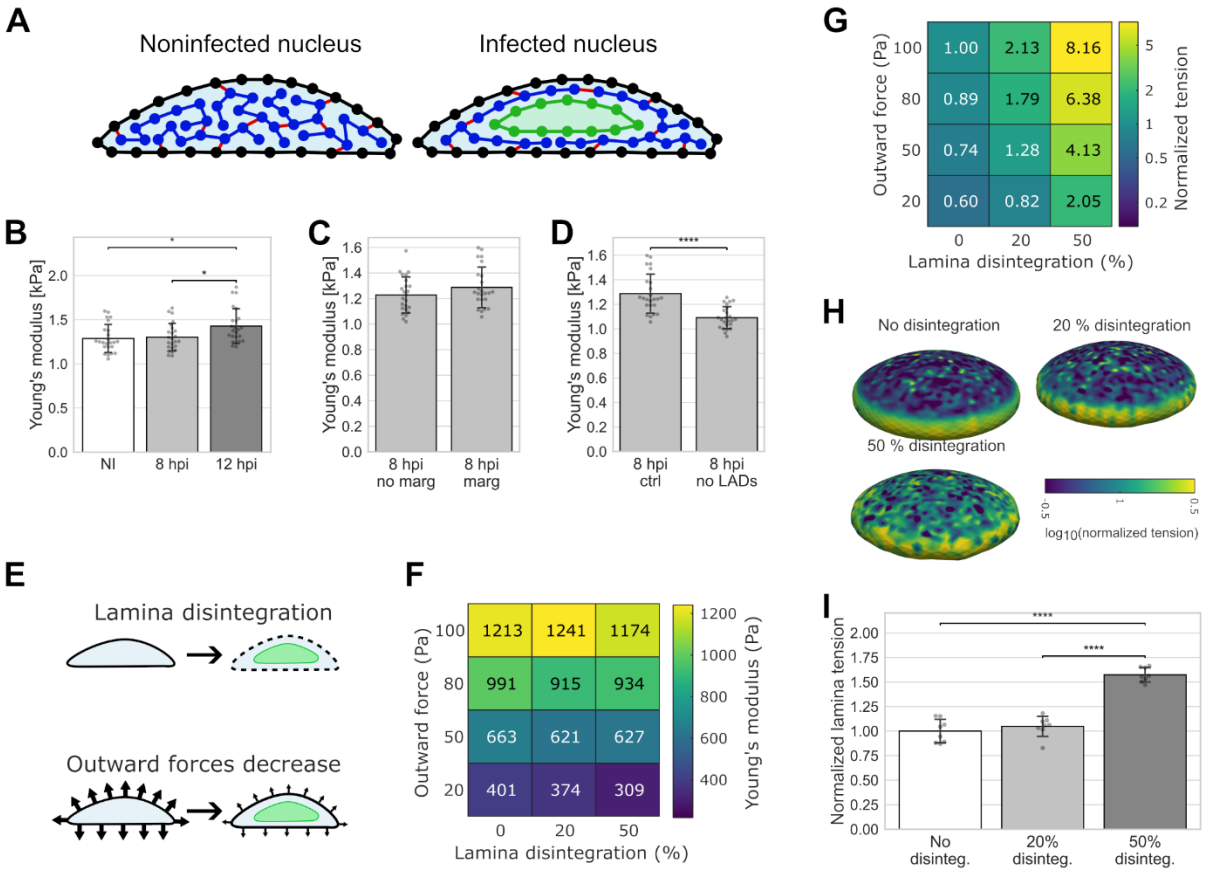

377 **Fig 5. Changes in mechanical parameters alter the nuclear stiffness. (A)** The setup for the
378 computational model shows a noninfected and an infected cell nucleus. The nuclear envelope
379 (black line), chromatin polymers (blue), envelope-chromatin and chromatin-chromatin
380 connections (red lines), and the viral replication compartment (green line) are shown. **(B)**
381 Simulated Young's moduli for the noninfected (NI) and infected cells (8 and 12 hpi), **(C)** for
382 the infected nuclei (8 hpi) without and with chromatin marginalization close to the nuclear
383 envelope, and **(D)** for the infected nuclei with and without lamina-associated domains (LADs)
384 (n=24). **(E)** Simulation of two changes in the nuclear mechanical parameters: lamina
385 disintegration and decrease in the outward forces. **(F)** Simulated Young's moduli as a function
386 of parameters in infected cell nuclei at 8 hpi (n=8). Significances are shown in S4 Fig. **(G)**
387 Normalized membrane tension as a function of lamina disintegration and outward forces (n=8).
388 Significances are shown in S4 Fig. **(H)** Representative examples of lamina forces with no
389 lamina disintegration and disintegration of 20% and 50%. **(I)** The sum of normalized lamina
390 forces on the top surface of the nuclei without or with 20% or 50% disintegration (normalized
391 to the mean value with no disintegration) (n=8). The error bars show the standard deviation.
392 Statistical significances were determined using Tukey's test (b, i) or Student's t-test (c, d), and
393 the significance values are denoted as **** ($p<0.0001$) or * ($p<0.05$). Nonsignificant
394 differences ($p \geq 0.05$) are not labeled.
395

396 # Intranuclear cytoskeletal pulling forces and cell-substrate contact
397 # area decrease in infection

398 Our computational modeling indicated that decreases in cytoskeletal pulling forces and osmotic
399 pressure reduce nuclear softness. Previous studies have shown that suppressing the LINC
400 complex protein SUN2 alters nuclear mechanical properties, leading to nuclear softening [23].
401 Consistent with our studies, the infection-induced decrease in SUN2 has been detected in HSV-

402 1 and human cytomegalovirus infections [57,58]. Nuclear Ca^{2+} ions are connected to the shape
403 regulation of the nucleus [59], nuclear translocation [60], and chromatin compaction [61].
404 Here, to monitor virus-induced nuclear changes and to verify the reliability of the model, we
405 performed experimental validation of mechanical force on the LINC complex and of nuclear
406 Ca^{2+} levels during infection.
407
408 First, we analyzed the effect of HSV-1 infection on the mechanical forces transmitted through
409 the cytoskeleton to the nucleus. Here, we used a nesprin FRET tension sensor with a phasor
410 approach to FLIM to measure the force on the LINC complex [62]. These studies indicated that
411 the cytoskeletal pulling force of the nucleus was significantly lower in infected Vero cells at 8
412 and 12 hpi compared to noninfected cells (Figs. 6A and B, see also S5 Fig). This demonstrates
413 that the mechanical linkage of the cytoskeleton to the nucleus is altered in infection, and the
414 LINC complex forces decrease.
415
416 Next, we labeled cells for beta actin and measured their contact areas to the substrate in
417 noninfected and infected cells. The analysis revealed that the cell contact area was reduced
418 during infection (Figs 6C and D). This supports the idea that a decrease in outward forces due
419 to reduced actin cytoskeleton pull occurs during the infection.
420
421 Finally, we measured nuclear Ca^{2+} concentration using phasor analysis for FLIM of single-
422 molecule calcium biosensor G-Ca-FLITS [63,64]. The data show that nuclear Ca^{2+}
423 concentration is lower in infected Vero cells at 8 and 12 hpi than in noninfected cells (Figs 6E
424 and F, see also S6 Fig). Altogether, the reduced nuclear Ca^{2+} concentration suggests that
425 chromatin compaction may decrease in infection, which probably affects nuclear mechanics.

426

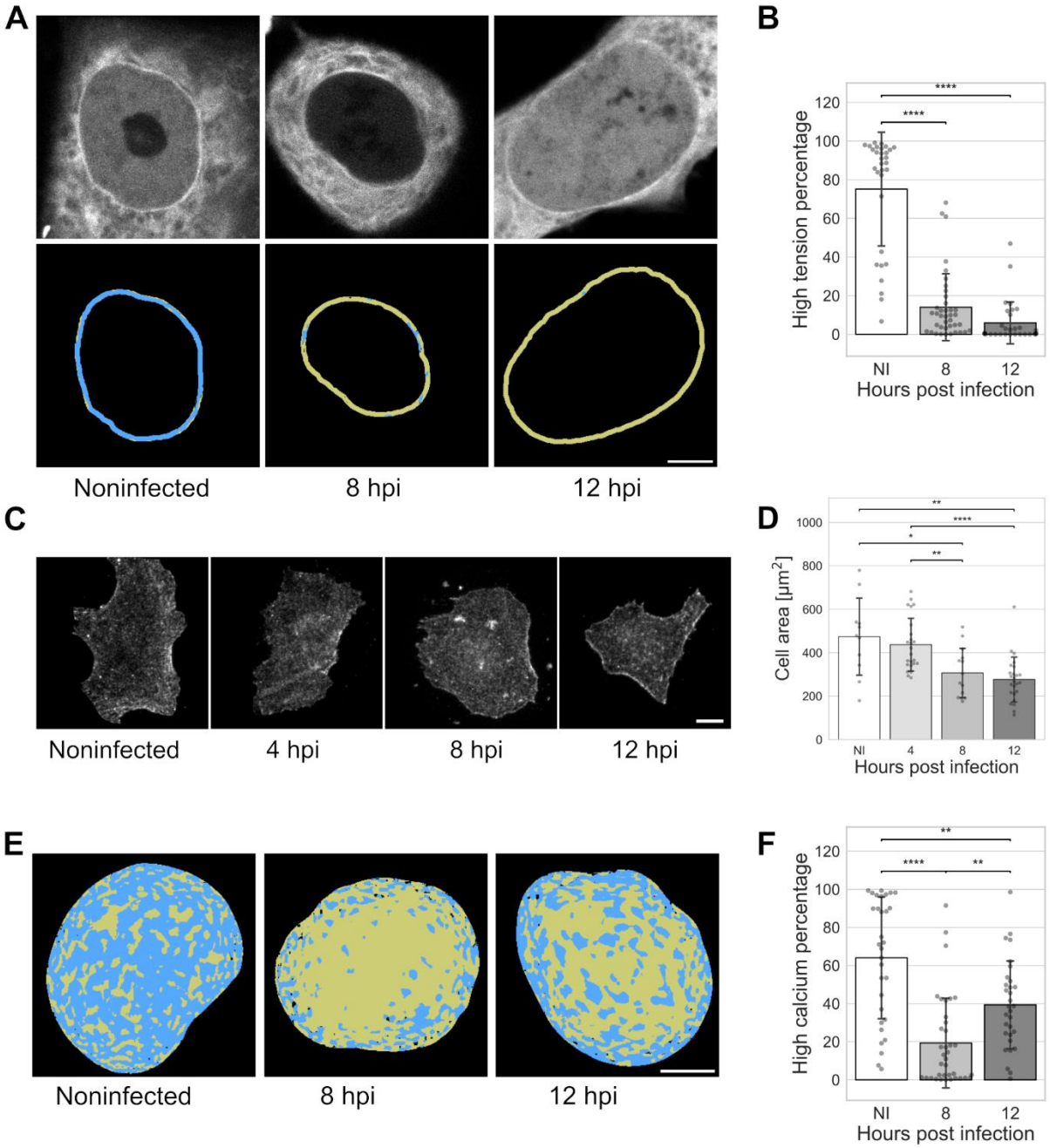

427

428 **Figure 6. Cytoskeletal forces on the nucleus decrease in infection. (A)** The nesprin tension
429 FRET sensor analysis of the cytoskeletal pulling force in noninfected and infected Vero cells
430 at 8 and 12 hpi. FRET donor fluorescence intensity (grey) and nesprin tension, quantified from
431 the donor lifetime (S5 Fig), divided into low (yellow) and high (blue) tension regions at the
432 segmented nuclear envelope. Scale bar, 5 µm. **(B)** The percentage of high tension regions in
433 the segmented nuclear membrane in noninfected (NI) and infected cells at 8 and 12 hpi (n=31,

434 39, and 31, respectively). **(C)** Sum projection of beta-actin immunolabeled noninfected and
435 infected cells at 4, 8, and 12 hpi. Scale bar, 10 μm. **(D)** The measurement of the area covered
436 by noninfected and infected cells at 4, 8, and 12 hpi (n = 11, 24, 14, and 25, respectively). **(E)**
437 Phasor FLIM analysis of calcium concentration using a single-molecule calcium biosensor in
438 noninfected and infected Vero cells at 8 and 12 hpi. The calcium concentration in the nucleus
439 divided into low (yellow) and high concentration (blue) regions according to each pixel´s
440 fluorescence lifetime distribution in the phasor plot (S6 Fig). Scale bar, 5 μm. **(F)** The
441 percentage of high calcium concentration regions of the total nuclear region in noninfected
442 cells and infected cells at 8 and 12 hpi (n=31, 37, and 31, respectively). The error bars show
443 the standard deviation. Statistical significance was determined using Tukey's test, and the
444 significance values are denoted as **** ($p<0.0001$), ** ($p<0.01$), or * ($p<0.05$). Nonsignificant
445 differences ($p \geqslant 0.05$) are not labeled.

446

447 # Discussion

448 Previous studies on isolated nuclei have shown that nuclear stiffness increases after the nuclear
449 injection of the HSV-1 genome [65]. Our data shows that this is a transitory phenomenon or
450 specific to isolated nuclei since the progression of the infection in living cells led to nuclear
451 softening. The observed softening could be explained by changes in nuclear structure caused
452 by the enlarged VRC at the center of the nucleus, changes in the nuclear lamina and chromatin,
453 a decrease in the external pull from the cytoskeleton, or a decrease in osmotic pressure.

454

455 The progression of HSV-1 infection leads to an enlarged nuclear VRC, and at the late stages
456 of infection, the VRC can occupy one-third of the nuclear volume [28]. Our SXT results

457 indicate that the VRC region is less dense than the euchromatin region in noninfected cells and
458 the marginalized chromatin in infected cells. This shows that HSV-1 infection forms an
459 expanded low-density nuclear center surrounded by chromatin. It has been demonstrated that
460 particle density is proportional to stiffness in many materials, such as collagen-based hydrogels
461 [66,67]. While other factors, such as crosslink density between hydrogel fibers [68], also
462 influence stiffness, the lower density of the VRC may indicate lower stiffness than chromatin
463 and contribute to nuclear softening during infection. It has remained unclear how the infection
464 and the enlarged VRC affect intranuclear ion and osmotic concentration. Modeling has stated
465 that nuclear osmotic pressure is proportional to the macromolecular concentration [69,70].
466 Thus, the reduced macromolecular concentration in the VRC region likely contributes to
467 regulating nuclear stiffness by decreasing osmotic pressure.
468
469 One of the major regulators of nuclear stiffness is the nuclear lamina associated with peripheral
470 heterochromatin, particularly lamins A and C [10,12,13,71–74]. Studies with lamin A/C-
471 deficient yeast cells have shown that chromatin tethering to the nuclear membrane increases
472 the mechanical stiffness of the NE, and untethering of the chromatin leads to a softer nucleus
473 [7]. In HSV-1 infection, nuclear softness may be altered by virus-induced modification of the
474 nuclear lamina. Herpesvirus infection does not change the expression of lamins, but results in
475 local dispersion of the nuclear lamina by phosphorylation and redistribution of lamins A/C and
476 B. Various viral proteins and kinases (UL13, UL34, ICP34.5, and Us3) mediate these processes
477 [39,75–78]. We showed how the mobility of the nuclear lamina decreases in infection,
478 suggesting a possible increase in its tension or rigidity. However, it cannot be ruled out that
479 infection-induced changes in the microtubules might also play a role in NE mobility [7]. Our
480 simulations showed that the effect of lamina disintegration alone was not significant on
481 simulated nuclear stiffness. Still, it became relevant when the outward forces, described as the

482 combined effect of cytoskeletal pulling forces and osmotic pressure on the NE, were reduced.
483 Finally, we showed that nuclear membrane tension increases at late infection, coinciding with
484 nuclear volume expansion. This could be explained by earlier studies showing that nuclear
485 swelling induces mechanical stretching forces that elevate membrane tension [79]. Membrane
486 tension could also be affected by changes in lipid deformation during the formation of the viral
487 egress complex [80]. Our simulations showed that the disintegration of the lamina led to
488 increased membrane tension even when outward forces were reduced, because more of the
489 outward forces were subjected to the membrane rather than to the lamina.
490
491 Our simulations were conducted to explain the experimental softening of the nucleus. They
492 indicated that a reduction in outward forces led to the most significant decrease in nuclear
493 stiffness, suggesting this could be the primary mechanism underlying the experimentally
494 observed change in nuclear stiffness during the infection. The outward forces described the
495 combined effects of cytoskeletal forces on the NE and osmotic pressure in the nucleus. Nuclear
496 elasticity is partly regulated by the cytoskeletal tension mediated by the LINC complex, which
497 links the nucleo- and cytoskeleton [10,74,12]. Our data showed that the force transmission from
498 the cytoskeleton to the nucleus is altered in HSV-1 infection. First, we observed that SUN2
499 expression decreases during HSV-1 infection. Suppressing LINC protein SUN2 changes the
500 mechanical properties of the nucleus and causes nuclear softening [23]. In macrophages, a
501 deficiency of SUN1 and SUN2 proteins causes a decrease in nuclear size and an increase in
502 nuclear elasticity [81]. SUN2 is a short-lived protein with a degradation half-life of 240 min
503 [82], and temporal proteomics analysis has confirmed the reduced amount of SUN2 at late
504 HSV-1 infection [57]. This most likely regulates the mechanical properties of the nucleus and
505 reduces nuclear stiffness as the infection progresses. However, it cannot be the sole effector,
506 since nuclear stiffness is already lower at 4 hpi, when SUN2 has not yet been downregulated.

507 SUN2 depletion also modifies the NE double membrane and the perinuclear space [82,83].
508 Second, we showed that tension on nesprin proteins decreases in the infection. It is known that
509 the force on the LINC complex can directly affect nuclear elasticity, and a decrease in the
510 cytoskeletal pull softens the nucleus [22,23]. Additionally, it is known that HSV-1 rearranges
511 the actin cytoskeleton via cofilin-1 [84]. Finally, we observed that the cell-substrate contact
512 area decreased during infection, supporting the observed reduction in cytoskeletal tension [85].
513 Together, the downregulation of SUN2, the observed decrease in cell-substrate contact area,
514 and the reduced force on the LINC complex indicate that the cytoskeletal pulling force on the
515 nucleus was reduced.
516
517 The subdiffusive capsid motion in the nucleus is restricted by chromatin marginalized toward
518 the NE. However, later in infection, the chromatin barrier becomes more permissive, and the
519 probability of capsids entering the chromatin increases [33]. The mechanical changes that we
520 observed might partly explain this phenomenon. Specifically, downregulation of the SUN
521 protein has been shown to reduce chromatin condensation [86]. In HSV-1 infection, decreased
522 SUN2 expression could facilitate the progression of infection and the nuclear egress of HSV-
523 1 capsids, possibly by remodeling chromatin and NE organization [87]. The recent
524 cytomegalovirus data show that changes in LINC-complex-mediated microtubule
525 mechanotransduction lead to reorganization of both hetero- and euchromatin [88]. Moreover,
526 nuclear chromatin compaction is also regulated by Ca^{2+} ion concentration. At low calcium
527 levels, the negative charges of DNA remain partially unneutralized, leading to more expanded
528 fibrous chromatin [61]. The lower calcium concentration that we observed during infection
529 may therefore trigger local remodeling and decondensation of chromatin and possibly affect
530 chromatin dynamics, which could explain the facilitated capsid diffusion through the chromatin
531 during the nuclear egress of viral capsids. The decreasing calcium concentration also suggests

532 that intranuclear osmotic pressure may decrease during infection. However, calcium is only
533 one of the many ions and molecules that affect osmotic pressure, and we cannot make
534 conclusions based solely on it. Moreover, due to the NLS-tagged sensor we used, we cannot
535 assess the difference in calcium concentration between the nucleus and the cytoplasm.
536
537 In summary, herpesvirus infection and the emergence of enlarged, low-density VRCs lead to
538 changes in nuclear volume, organization of chromatin and the nuclear lamina, and the
539 connections to the cytoskeleton. Virus-induced nuclear deformation alters the nuclear
540 environment and triggers changes in the intrinsic forces acting on the nucleus (Fig 7).
541 Altogether, these profound changes cause nuclear softening. Our simulations show that the
542 measured changes in the nuclear lamina and size have a relatively minor effect on stiffness
543 compared to nucleocytoplasmic forces, namely cytoskeletal-nuclear connections and osmotic
544 pressure. While the reorganization of the lamina is known to be essential for the nuclear egress
545 of new HSV-1 viral capsids, the role of the predicted reduction in nucleocytoplasmic forces
546 during infection remains elusive. Changes in the osmotic balance between the nucleus and the
547 cytoplasm can, for example, originate from changes in nuclear transport, which HSV-1-
548 induced changes in the nuclear pore function could cause [89]. These emerging insights shed
549 new light on the virus-induced fundamental remodeling of nuclear organization and
550 mechanobiology, and their impact on the progression of HSV-1 infection.
551

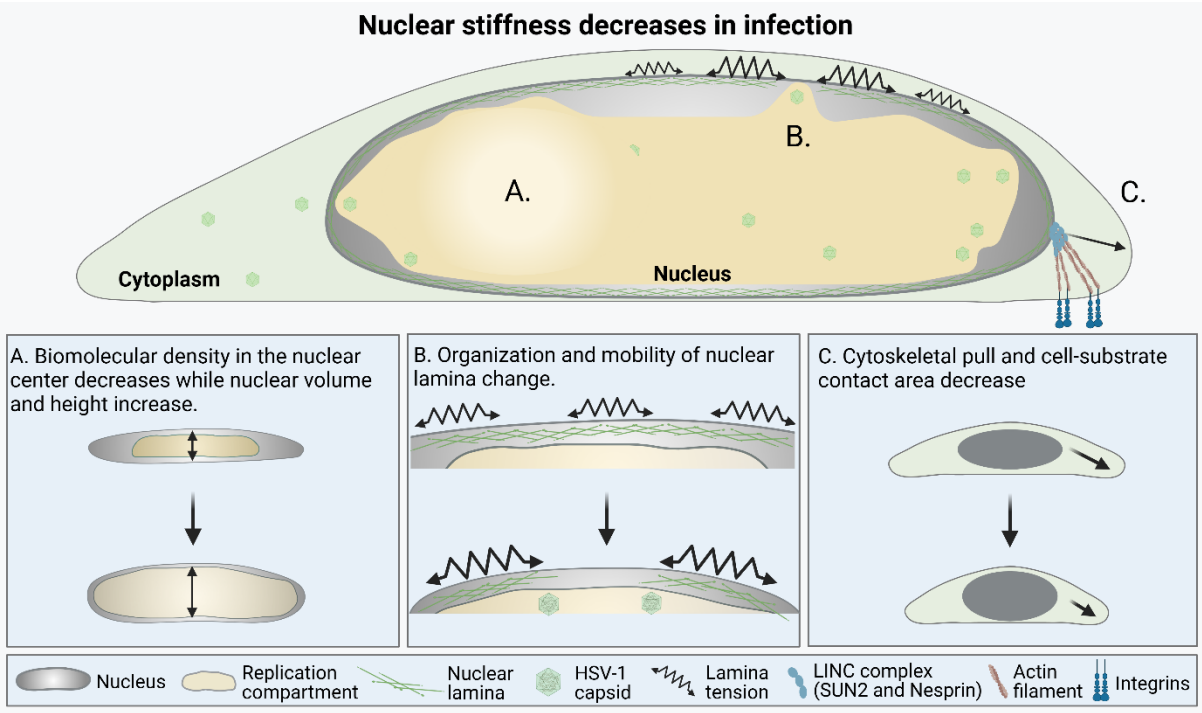

Fig 7. Virus-induced changes in mechanical forces regulating nuclear stiffness. HSV-1 infection leads to extensive changes in nuclear organization and mechanical forces. **(A)** The infection results in an enlarged nuclear viral replication compartment, a low-density area surrounded by a condensed chromatin layer. **(B)** Changes in the organization and mobility of the nuclear lamina accompany the increase in nuclear volume and height. **(C)** Nuclear stiffness is affected by cytoskeletal pull. The key regulator of cytoskeletal tension of the nucleus, LINC complex protein SUN2, is strongly downregulated in infection, and nesprin tension decreases together with the cell-substrate contact area. Viral infection alters the mechanical properties of the nucleus and leads to nuclear softening.

Materials and Methods

564 ## Cells and viruses

565 Mouse embryonic fibroblast cells (MEF, ATCC® CRL-2991™) and African green monkey
566 kidney cells (Vero, ATCC® CCL-81™) were grown in Dulbecco's modified Eagle medium
567 (DMEM) supplemented with 10% fetal bovine serum, L-glutamine, and penicillin-
568 streptomycin (Gibco-Invitrogen, Carlsbad, CA) at 37 °C in the presence of 5% CO_2. HA-tagged
569 progerin, a truncated form of lamin A [90], was expressed in Vero cells using adenovirus [91].
570 Lamin A adenovirus was used to overexpress wild-type lamin A in Veros. Lamin A adenovirus
571 (based on RefSeq BC014507) was purchased from Vector Biolabs and used as previously
572 described [91]. The cells were infected 4, 8, or 12 hours before imaging and measurements with
573 the wild-type 17+ strain, EYFP-ICP4 (vEYFP-ICP4 [92]), or VP26-mCherry virus
574 (HSV1(17^+)Lox-CheVP26 [93–95]) at a multiplicity of infection of 5.
575

576 ## Atomic force microscopy (AFM)

577 Force spectroscopy AFM experiments were performed on noninfected and infected Vero cells
578 at 4, 8, and 10 hpi using a NanoWizard 4 XP instrument (JPK BioAFM, Bruker Nano GmbH,
579 Berlin, Germany) mounted on an inverted microscope (Nikon Ti-U, Nikon Instruments Europe
580 B.V., Amsterdam, the Netherlands) equipped with a standard monochrome CCD camera
581 (ProgRes MFCool, Jenoptik, Jena, Germany). Fluorescence imaging was performed using
582 wide-field illumination (Intensilight Hg lamp, Nikon) with a 100X objective (Nikon CFI Apo
583 VC, 1.4 NA, oil immersion) and the appropriate filter cube for EYFP. A software module
584 (DirectOverlay, JPK Bio-AFM, Bruker Nano GmbH, Berlin, Germany) calibrated the tip
585 position with the optical image. Nanomechanical measurements were performed in
586 spectroscopy mode using a 6.62 µm probe (CP-PNPL-SiO-C from SQube, mean cantilever
587 spring constant $k_{cant} = 0.06$ N/m). Before each set of acquisitions, the sensitivity and spring
588 constant of the cantilever were calibrated (thermal noise method). The measurements were

589 performed in buffered culture medium at 37°C under 5% CO2, with a relative setpoint of 2 nN,
590 a Z-length of 12 µm, and a constant extension velocity of 1 µm/s. The center of the nucleus of
591 a cell was visualized by fluorescence, and ten successive force curve measurements were taken.
592 Raw data were cleaned manually by removing any aberrant contact points, and each force curve
593 was fitted with a Hertz model to calculate Young's modulus using JPK data Processing
594 software (7.0.181). The average pressing depth ranged from 0.9 µm (noninfected) to 3.3 µm
595 (10 hpi), as analyzed by randomly selecting about 50% of cells at each infection time point.
596 This reflects the decrease in nuclear stiffness that occurs during the infection. The average
597 measures were plotted by cell (one point is one cell) after filtering out outliers (z-score>3).
598

599 Cryo-soft X-ray tomography (SXT) of suspended cells in 600 capillaries

601 MEF cells were seeded into culture flasks (Corning, Corning, NY) and infected with HSV-1
602 vEYFP-ICP4 at an MOI of 5 for 4 and 8 hours at 37°C. Noninfected and infected cells were
603 detached with trypsin-EDTA, pelleted by centrifugation (300x*g*), and washed with PBS. Cells
604 were then fixed with glutaraldehyde (0.5%) and paraformaldehyde for 10 minutes at RT and
605 35 minutes at 4°C (4%, cat. No. 15713-S; Electron Microscopy Sciences, Hatfield, PA),
606 washed once with PBS, pelleted by centrifugation (300x*g*), re-suspended in the PBS buffer,
607 filtered, loaded into thin-walled cylindrical borosilicate glass capillaries (Hilgenberg GmbH,
608 Hilgenberg, GER, Cat. No. 4023088), and then vitrified by quickly plunging them into liquid-
609 nitrogen-cooled (~90 K) liquid propane. SXT tomographic data were collected by full-rotation
610 imaging with a soft X-ray microscope (XM-2) in the National Center for X-ray Tomography
611 at the Advanced Light Source (http://www.als.lbl.gov) of Lawrence Berkeley National
612 Laboratory (Berkeley, CA). Cells were kept in a stream of liquid-nitrogen-cooled helium gas
613 to avoid radiation damage during data collection. For each data set, 180° rotation tomographs

614 (1 projection image per 2° angle) were collected [96,97]. Projection images were aligned by
615 tracking fiducial markers and reconstructed using automatic reconstruction software [98]. The
616 high- and low-density chromatin was segmented using histogram-based separation into two
617 classes in Dragonfly (Comet Technologies Canada Inc., Montreal, Canada).
618

619 Focused Ion Beam Scanning Electron Microscopy (FIB-SEM)

620 The volume imaging data set of MEF cells with enhanced chromatin contrast was generated
621 using FIB-SEM. MEFs, noninfected or HSV-1 infected at an MOI of 5 for 8 h, were processed
622 for imaging as described earlier [99]. The Chrom EM method was used to enhance the contrast
623 of DNA [45]. The deposition of the osmiophilic polymer of diaminobenzidine, specifically on
624 the DNA, was carried out using the fluorescent emission of DRAQ5. For this, the cells were
625 placed on a cooled stage of a Leica DM IL LED microscope and exposed to 620 $\pm$ 30 nm light
626 in the presence of diaminobenzidine, inducing its local polymerization over DRAQ5-bound
627 DNA. The cells were treated with osmium tetroxide, followed by dehydration in a graded series
628 of ethanol and embedding in resin. One set of cells was thin-sectioned and then poststained
629 with 2% uranyl acetate and lead citrate. Another set of cells was coated with platinum. The
630 sections were imaged using a Jeol JEM-1400HC transmission electron microscope with an
631 Olympus SIS Quemesa bottom-mounted CCD camera (80 kV). The datasets were acquired in
632 a Zeiss Crossbeam 500 using backscattered and secondary electron signals. The area of interest
633 was exposed using a milling beam (0.7 nA at 30 kV) and imaged with a scanning electron beam
634 (0.31 or 0.50 nA, 1.5 or 1.6 keV). The milling and scanning process of the cell cross-section
635 produced an image volume with a voxel size of 2.5 x 2.5 x 5 nm^3. The datasets were collected
636 and aligned using Zeiss Atlas 5 software with a 3D tomography module. Microscopy Image
637 Browser [100] was used to segment the capsids, chromatin, and the NE. The chromatin
638 segmentation was done semi-automatically using MIB (https://mib.helsinki.fi/) and cleaned

639 using iterative intensity-based erosion. The local thickness of the chromatin was measured in
640 ImageJ (https://imagej.net/imagej-wiki-static/Local_Thickness) using Python; local maxima
641 were identified, and the local thickness value was extracted. The distance of these local maxima
642 to the NE was then calculated using the Euclidean distance transform.
643

644 Confocal imaging and analysis

645 Wild-type Vero cells, Vero cells expressing HA-tagged progerin, or Vero cells overexpressing
646 wild-type lamin A were grown on glass coverslips for microscopy to analyze nuclear volume.
647 The cells were infected with HSV-1 EYFP-ICP4 and fixed at 8 and 12 hpi with 4% PFA, and
648 DNA was labeled with DAPI. Viral EYFP-ICP4 was boosted with an anti-GFP antibody. Cells
649 were embedded into VECTASHIELD® PLUS Antifade Mounting Medium (H-1900) (Vector
650 Laboratories). The cells were imaged using a Leica SP8 confocal microscope with a UPLSAPO
651 63x oil immersion objective (NA 1.35). DAPI (Invitrogen) was excited with a 405 nm diode
652 laser, and a 410-439 nm band-pass filter was used to detect fluorescence. EYFP was excited
653 with a 488 nm laser, and the fluorescence was collected with a 519-540 nm bandpass filter.
654 Lamin A/C was excited with a 653 nm laser, and fluorescence was collected with a 661-839
655 nm filter. Stacks of 1024 x 1024 pixels were collected with a 120 nm/pixel pixel size in the x-
656 and y- directions and 400 nm in the z-direction. The nuclei were segmented using the minimum
657 cross-entropy threshold algorithm [101] for the DAPI channel.
658

659 For analyses of the nuclear intensity of lamins, Vero cells infected with HSV-1 EYFP-ICP4
660 and fixed at 8 and 12 hpi were labeled with antibodies against lamin A/C (mouse monoclonal
661 antibody MAb; ab8984, Abcam, Cambridge, UK) and Lamin B1 (rabbit polyclonal antibody,
662 rAb; ab16048, Abcam). The primary antibodies were followed by goat anti-rabbit or anti-
663 mouse Alexa 546- (lamin A/C) and 647- (lamin B1) conjugated secondary antibodies (Thermo

664 Fisher Scientific, Waltham, MA, USA). DNA was labeled with Hoechst 1:10000 in PBS for
665 10 min. Cells were embedded into VECTASHIELD® PLUS Antifade Mounting Medium (H-
666 1900) (Vector Laboratories). The immunolabeled cells were imaged using a Leica TCS SP8
667 FALCON laser scanning confocal microscope (Leica Microsystems, Mannheim, Germany).
668 Alexa 546 and Alexa 647 were excited with 557 nm and 653 nm wavelengths of pulsed white
669 light laser (80 MHz), respectively. The emission detection range was 568-648 nm for Alexa
670 546 and 663-776 nm for Alexa 647. DAPI was excited with a 405 nm diode laser, and emission
671 between 415-495 nm was detected. Laser powers for all channels were fixed. Stacks of 1024 x
672 1024 pixels were collected with 120 nm/pixel in the x- and y- directions and 240 nm in the z-
673 direction. The nuclei were segmented using a minimum cross-entropy threshold algorithm
674 [101] for the DAPI channel. The total nuclear intensity was calculated for the pixels belonging
675 to the segmented nucleus, and the intensity near the NE was calculated by using only pixels
676 having an Euclidean distance of 1 μm or less from the NE.
677
678 The distribution and mobility of lamins were imaged in living noninfected and HSV-1
679 mCherry-infected (8 and 12 hpi) Vero cells transfected with lamin A/C-Chromobody-GFP2
680 (Proteintech, Manchester, UK) by electroporation using Neon Transfection System (Thermo
681 Fischer Scientific) with 1150 V and two pulses with a width of 20 ms. Before imaging, the
682 cells were labeled with 1 μM Hoechst 33342. During the imaging with Leica SP8 Falcon, using
683 Leica HC PL APO CS2 1.2NA 63X water immersion objective, Hoechst was excited with 405
684 nm laser, 1% laser power and the emission collected between 412-475 nm (HyD), the lamin
685 A/C-Chromobody-GFP2 was excited with a 488 nm wavelength of white light laser, 10% laser
686 power and the emission was collected between 495-560 nm (HyD), and the mCherry channel
687 was excited using 587 nm, 10% laser power and emission was collected between 594-800 nm
688 (HyD). The image size was 296 x 296 pixels with a 100 nm pixel size in the x- and y-directions

689 and the imaging speed was bidirectional 1000 Hz with two sequences (1. Hoechst, 2. GFP and
690 mCherry), resulting in 3.2 frames per second for 60 seconds. The lamina was analyzed by first
691 removing its translational and rotational motion. The lamina was skeletonized at each time
692 point, and the maximumintensity projection of the skeletons was taken. The area of the
693 maximum intensity projection was calculated and divided by its length. The curvature was
694 defined by discretizing the nuclear lamina using 16-pixel (1.6 μm) long line segments and
695 calculating the angles between consecutive segments.
696
697 To measure the contact area of the cells during the infection, ICP4-EYFP-infected cells were
698 labeled using a mouse Anti-beta Actin antibody ([mAbcam 8226], Abcam). The contact area
699 of the cells during the infection was analyzed by taking the sum projection of the actin channel
700 along the z-direction, thresholding the sum projection using the minimum cross-entropy
701 algorithm [101], and calculating the area of the segmented region.
702

703 Fluorescence lifetime imaging and analysis

704 Nuclear membrane tension was analyzed by FLIM using fluorescent membrane tension probe
705 ER Flipper-TR® (Spirochrome) in noninfected and HSV-1 17+ wt infected live Vero cells at 8
706 and 12 hpi. Measurements were performed with a Leica SP8 Falcon using Leica HyD SMD
707 detectors and a Leica HC PL APO CS2 1.2NA 63X water immersion objective. The ER Flipper
708 probe was used at 1 μM, and the cells were also labeled with Hoechst 33342 at 1 μM. One
709 plane at the center of the nucleus, where the nuclear edges were clearly visible, was first
710 acquired with 405 nm excitation and 415-465 nm emission to visualize DNA with Hoechst.
711 Immediately after, the ER Flipper was imaged using 477 nm excitation and 550-650 nm
712 emission, and line accumulation of 16. The scanning speed was 200 Hz, the repetition rate was
713 80 MHz, and the image size was 328x328 pixels with 81x81nm/pixel for both Hoechst and ER

714 Flipper imaging. For tension analysis, pixel binning of 3 was used, resulting in approximately
715 500-1500 photons per pixel. After binning, a pixel-wise two-component fitting was performed,
716 and the longer component, corresponding to membrane tension, was extracted. Using the
717 Hoechst data, a 486 nm wide ring just outside the cellular DNA was used as a mask to obtain
718 the nuclear membrane area from the tension data. The mean of the longer ER Flipper lifetime
719 along the NE was calculated for each cell.
720
721 Pcdna nesprin TS, a gift from Daniel Conway (Addgene plasmid #68127;
722 http://n2t.net/addgene:68127; RRID: Addgene #68127), was used to measure the amount of
723 cytoskeleton tension towards the nucleus, reported by FRET, across the nuclear envelope. The
724 Vero cells were transiently transfected by electroporation using the Neon Transfection System
725 (Thermo Fischer Scientific) with two 1150 V pulses of 20 ms width, and grown overnight on
726 a 35 mm live-imaging glass-bottom dish (Ibidi) in an antibiotic-free medium. The next day, or
727 the day after, the cells were mock-infected and infected with HSV-1 VP26-mCherry, and
728 imaged at 8hpi and 12hpi using a Leica SP8 Falcon at 37°C and 5% CO_2, with a Leica HC PL
729 APO CS2 1.2NA 63X water immersion objective. Before starting the imaging, the medium
730 was changed to one without phenol red and containing 1 µM Hoechst 33342. All imaging was
731 conducted approximately between 30 minutes before and 30 minutes after the designated time
732 points, and the mock-infected cells were imaged in between the two time points. Mock-infected
733 and infected cells were made from the same set of transfected cells for two biological replicates,
734 and a third biological replicate of mock-infected cells was imaged for more n. From each
735 imaged cell, first a reference image was taken from Hoechst (excitation 405nm, 1% laser
736 power, emission 415-473nm, PMT), nesprin TS donor (excitation 470nm, 3% laser power,
737 emission 485-500nm, HyD photon counting), nesprin TS acceptor (excitation 514nm, 3% laser
738 power, emission 520-580nm, HyD photon counting) and mCherry (excitation 580nm, 3% laser

739 power, emission 600-700nm, HyD photon counting) in four sequences, after which the FLIM-
740 FRET data was acquired for the nesprin TS donor channel for 1 minute using frame repetition
741 at the speed of 700 Hz and 80MHz pulse rate. Only cells with >50 photons per pixel at the NE
742 were included in the analysis, as they provided a precise phasor cloud distribution without
743 significant background contribution using the LAS X wavelet filter. On the other hand, cells
744 with >1500 photons in the brightest pixel were excluded as the data was dominated by the high
745 FRET of overexpressed non-bound nesprin TS. A pixel size of 69 nm (x,y), an image size of
746 360 (x,y) pixels, and a pinhole of 1 airy unit were used. An ROI for the NE was generated by
747 automatic thresholding of nesprin TS FLIM or intensity data, or by manually drawing the NE
748 in ImageJ. The data were divided into low- and high-FRET pixels at the NE, which inversely
749 reports for high and low tension, respectively. A FRET efficiency threshold of 10% was used
750 for the division. The number of pixels with low and high FRET at the NE was quantified for
751 each cell, inversely representing the tension between the nucleus and cytoskeleton. A
752 description of the phasor FLIM-FRET analysis workflow is presented in the S5 Fig.
753
754 To measure intranuclear calcium concentration, we used 3xnls-G-Ca-FLITS, a gift from Dorus
755 Gadella (Addgene plasmid #191463; http://n2t.net/addgene:191463; RRID: Addgene
756 #191463). The Vero cells were transiently transfected by electroporation using the Neon
757 Transfection System (Thermo Fischer Scientific) with two 1150 V pulses of 20 ms width, and
758 grown overnight on a 35mm live-imaging glass-bottom dish (Ibidi) in an antibiotic-free
759 medium. The next day, or the day after, the cells were mock-infected and infected with HSV-
760 1 VP26-mCherry, and imaged at 8hpi and 12hpi using Leica SP8 Falcon at 37°C and 5% CO_2
761 and Leica HC PL APO CS2 1.2NA 63X water immersion objective. Before starting the
762 imaging, the medium was changed to one without phenol red and containing 1 μM Hoechst
763 33342. All imaging was conducted approximately between 30 minutes before and 30 minutes

764 after the designated time points, and the mock-infected cells were imaged in between the two
765 time points. Mock-infected and infected cells were generated from the same set of transfected
766 cells, with two biological replicates. The FLIM data were acquired by exciting the G-Ca-FLITS
767 biosensor with a 474 nm laser at 3% power and 40 MHz repetition rate, for 1 minute at the
768 speed of 1800 Hz. For increased photon detection rate, the emission spectrum was divided into
769 two HyDs, first detecting 490nm-534nm and second 540-580nm, resulting in >400 photons per
770 pixel. The 5 nm gap in the detection spectrum was because a PMT detector is placed in between
771 the two HyDs in the system. Simultaneously to acquiring the G-Ca-FLITS FLIM data, Hoechst
772 33342 (excitation 405, laser power 0.5%, emission 415-490nm, PMT) and mCherry (excitation
773 586 nm, laser power 3%, emission 600-700nm, HyD) were acquired in separate sequences. A
774 pixel size of 68 nm (x,y), an image size of 306 pixels (x,y), and a 1 Airy unit pinhole size were
775 used. First, a control experiment was conducted with transfected noninfected cells, in which,
776 during live FLIM acquisition, the medium was supplemented with 5X ionomycin (From
777 APExBIO kit 2061). From this experiment, a calibration phasor FLIM line spanning low-to-
778 high calcium concentrations could be generated, confirming the expected sensor function.
779 Next, the phasor analysis of the biosensor FLIM data of noninfected and infected cells showed
780 a clear lifetime difference along the ionomycin calibration experiment. Phasor cursors were
781 drawn for these lifetime species to quantify nuclear pixels into high- or low-calcium
782 concentration groups according to their fluorescence lifetime. The ratio of high and low-
783 calcium concentration pixels for each nucleus was quantified. The phasor analysis of the G-
784 Ca-FLITS FLIM data is further described in S6 Fig.
785

786 ## Global Run-On and sequencing (GRO-seq)

787 GRO-seq analysis was performed as described previously [99]. Briefly, to prepare nuclei,
788 noninfected and infected Vero cells (at 4 and 8 hpi) were swollen, and the nuclei were collected
789 and stored at -80°C. The preparation of GRO-Seq libraries followed the previously described
790 protocol [99,102]. The library quantification was performed using a Qubit fluorometer
791 (Thermo Fisher Scientific) and prepared for 50 bp single-end sequencing on an Illumina HiSeq
792 2000 platform (GeneCore, EMBL Heidelberg, Germany). The raw sequencing reads were
793 assessed by the FastQC tool (http://www.bioinformatics.babraham.ac.uk/projects/fastqc/) and
794 the FastX toolkit (http://hannonlab.cshl.edu/fastx_toolkit/). GRO-seq reads were aligned to the
795 ChlSab1.1 genome using the bowtie-0.12.7 software [103]. The best alignment was obtained
796 with up to two mismatches and up to three locations per read. Differentially expressed genes
797 were detected using ChlSab1.1.95.gtf coordinates, and the RNA.pl workflow of HOMER 4.3
798 and edgeR v3.2.2 were used for analysis. Genes were considered differentially expressed using
799 the following cutoffs: log2 fold change 0.585, RPKM 0.5 in at least one sample, and adjusted
800 p-value of 0.05. GRO-seq reads were mapped to the Human Protein Atlas
801 (https://www.proteinatlas.org/) to identify lamins and nuclear lamina-related proteins. The
802 interaction of these proteins was further mapped using the String database (https://string-
803 db.org/) by selecting experimentally shown interactions using a threshold of 500. The non-
804 interacting proteins were identified in the same String database, provided they interact with at
805 least one detected protein. The resulting graph was generated in Python using the networkx
806 package and then manually adjusted.

807 ## Western blot

808 0.7 x 10^6 Vero cells were plated on 5 cm cell culture dishes, grown over night, and infected the
809 next day with HSV-1 17+ wt (MOI 5). Noninfected and infected cells (8 hpi and 12 hpi)

810 weredetached by scraping. Scraped cells were collected in 1 ml of cold PBS and centrifuged at
811 2,000 x g for 5 min to pellet the cells. Cell pellets were resuspended in Laemmli sample buffer
812 containing 2.5% 2-mercaptoethanol (Bio-Rad Laboratories) in PBS and heated at 95 °C for 10
813 minutes. Protein standards (Bio-Rad Laboratories) and 15 µl of samples were loaded onto 4–
814 20% Mini Protean TGX Stain-Free gels (Bio-Rad Laboratories), and run at 100 V for 80
815 minutes. Total protein stain in the gels was activated for 5 min, and the gels were imaged to
816 detect the protein standards. Proteins were blotted onto 0.2 µm low fluorescence PVDF
817 membranes with the Trans-Blot Turbo RTA Transfer Kit (Bio-Rad Laboratories) and Trans-
818 Blot Turbo Transfer-System (Bio-Rad Laboratories). Blots and gels were imaged to verify
819 protein transfer. After acquiring the total protein stain for each blot the membranes were
820 blocked for 5 minutes in EveryBlot Blocking Buffer (Bio-Rad Laboratories, USA) and probed
821 with primary antibodies against SUN2 (ab124916, Abcam), Lamin A (ab26300,
822 AbcamPredicted band size: 74 kDa), Lamin B (ab16048, Abcam), and HSV-1 ICP4 (ab6514,
823 Abcam). Primary antibodies were detected using fluorophore-conjugated secondary antibodies
824 goat anti-mouse IgG StarBright Blue 520 and goat anti-rabbit IgG StarBright Blue 700 (Bio-
825 Rad Laboratories). Gels and immunoblots were imaged with the Bio-Rad ChemiDoc MP
826 Imaging System. Total band intensities for predicted-sized bands were quantified using Image
827 Lab 6.1 software (Bio-Rad Laboratories).
828

829 # Computational modeling

830 The developed computational model described the nucleus as an NE, including the nuclear
831 lamina, and chromatin components in three dimensions. The main model assumptions were:
832 (1) the mechanical properties of the nucleus are dictated by the nuclear envelope, chromatin,
833 and outward forces, including actin cytoskeleton prestress and osmotic pressure difference; (2)
834 no changes in the mechanical properties occur during the short AFM measurement; and (3) the

VRC has low density and has no effect on the AFM measurement. The NE was triangulated into a viscoelastic shell, and self-avoiding polymer chains were used to model the chromatin. Furthermore, additional interactions were defined to describe various connections, such as LADs between chromatin and the lamina, and between different parts of the chromatin. The herpesvirus VRC was described as a single coherent entity within the nucleus. It was represented similarly to the NE as a triangulated shape that repulses the chromatin as it grows.

The model was simulated by calculating a force affecting each vertex originating from various, usually Hookean, interactions and moving them using the damped equation of motion:

$$\gamma \vec{v}_i + \sum_j c_{ij} \left(\vec{v}_i - \vec{v}_j \right) = \vec{F}_i + \eta,$$

where γ is the system viscosity, $\vec{v}_i$ is the velocity of vertex i, c_{ij} is the friction between vertices i and j, $\vec{F}_i$ is the total force affecting vertex i, and η is the random thermal motion. The equation was solved using the conjugate gradient method, and the vertex movements were computed using the forward Euler method.

To simulate the AFM experiments, a cantilever with properties mirroring those of the one used in the experiments was used to push down on the nucleus, and the resulting force and indentation depth data were used to calculate the Young's modulus using the Hertz model. The computational model was implemented using Julia programming language (v1.10.2), and the model and the parameters are described in more detail in S1 Text. The code is available on GitHub (https://github.com/atervn/nuclear_mech) and Zenodo (https://zenodo.org/records/14512358). The data fitting for the Hertz model was done using Matlab (The MathWorks Inc, R2021a, Natick, Massachusetts) and 3D visualization using ParaView [104].

Data availability

The authors declare that the GRO-Seq data were deposited into the Gene Expression Omnibus database under accession number GSE243613 and are available at https://www.ncbi.nlm.nih.gov/geo/query/acc.cgi?acc=GSE243613. All other relevant data are in the manuscript and its supporting information files.

Acknowledgments

We thank the staff of the National Center for X-ray Tomography (NCXT) and Advanced Light Source (Lawrence Berkeley National Laboratory, Berkeley, CA) for providing cryo-SXT experiments. We also thank Helena Vihinen from the Electron Microscopy Unit (University of Helsinki, Institute of Biotechnology, Helsinki Institute of Life Science, Helsinki, Finland) for preparing and imaging FIB-SEM samples and Elina Mäntylä for preparing the GRO-Seq samples.

References

1. Uhler C, Shivashankar GV. Regulation of genome organization and gene expression by nuclear mechanotransduction. Nat Rev Mol Cell Biol. 2017 Dec;18(12):717–27.

2. Carley E, Stewart RM, Zieman A, Jalilian I, King DE, Zubek A, et al. The LINC complex transmits integrin-dependent tension to the nuclear lamina and represses epidermal differentiation. eLife. 10:e58541.

3. Versaevel M, Grevesse T, Gabriele S. Spatial coordination between cell and nuclear shape within micropatterned endothelial cells. Nat Commun. 2012 Feb 14;3:671.

4. Lammerding J. Mechanics of the nucleus. Compr Physiol. 2011 Apr;1(2):783–807.

883 5. Moore HM, Vartiainen MK. F-actin organizes the nucleus. Nat Cell Biol. 2017 Nov
884 29;19(12):1386–8.

885 6. Pajerowski JD, Dahl KN, Zhong FL, Sammak PJ, Discher DE. Physical plasticity of the
886 nucleus in stem cell differentiation. Proc Natl Acad Sci U S A. 2007 Oct
887 2;104(40):15619–24.

888 7. Schreiner SM, Koo PK, Zhao Y, Mochrie SGJ, King MC. The tethering of chromatin to
889 the nuclear envelope supports nuclear mechanics. Nat Commun. 2015 Jun 15;6:7159.

890 8. Turgay Y, Eibauer M, Goldman AE, Shimi T, Khayat M, Ben-Harush K, et al. The
891 molecular architecture of lamins in somatic cells. Nature. 2017 Mar 9;543(7644):261–4.

892 9. Vahabikashi A, Adam SA, Medalia O, Goldman RD. Nuclear lamins: Structure and
893 function in mechanobiology. APL Bioeng. 2022 Mar;6(1):011503.

894 10. Lammerding J, Schulze PC, Takahashi T, Kozlov S, Sullivan T, Kamm RD, et al. Lamin
895 A/C deficiency causes defective nuclear mechanics and mechanotransduction. J Clin
896 Invest. 2004 Feb;113(3):370–8.

897 11. Gruenbaum Y, Foisner R. Lamins: nuclear intermediate filament proteins with
898 fundamental functions in nuclear mechanics and genome regulation. Annu Rev Biochem.
899 2015;84:131–64.

900 12. Dahl KN, Kahn SM, Wilson KL, Discher DE. The nuclear envelope lamina network has
901 elasticity and a compressibility limit suggestive of a molecular shock absorber. J Cell Sci.
902 2004 Sep 15;117(Pt 20):4779–86.

903 13. Swift J, Ivanovska IL, Buxboim A, Harada T, Dingal PCDP, Pinter J, et al. Nuclear lamin-
904 A scales with tissue stiffness and enhances matrix-directed differentiation. Science. 2013
905 Aug 30;341(6149):1240104.

906 14. Ihalainen TO, Aires L, Herzog FA, Schwartlander R, Moeller J, Vogel V. Differential
907 basal-to-apical accessibility of lamin A/C epitopes in the nuclear lamina regulated by
908 changes in cytoskeletal tension. Nat Mater. 2015 Dec;14(12):1252–61.

909 15. Stephens AD, Banigan EJ, Adam SA, Goldman RD, Marko JF. Chromatin and lamin A
910 determine two different mechanical response regimes of the cell nucleus. Mol Biol Cell.
911 2017 Jul 7;28(14):1984–96.

912 16. Stephens AD, Liu PZ, Banigan EJ, Almassalha LM, Backman V, Adam SA, et al.
913 Chromatin histone modifications and rigidity affect nuclear morphology independent of
914 lamins. Mol Biol Cell. 2018 Jan 15;29(2):220–33.

915 17. Stephens AD, Liu PZ, Kandula V, Chen H, Almassalha LM, Herman C, et al.
916 Physicochemical mechanotransduction alters nuclear shape and mechanics via
917 heterochromatin formation. Mol Biol Cell. 2019 Aug 1;30(17):2320–30.

918 18. Mazumder A, Roopa T, Basu A, Mahadevan L, Shivashankar GV. Dynamics of
919 chromatin decondensation reveals the structural integrity of a mechanically prestressed
920 nucleus. Biophys J. 2008 Sep 15;95(6):3028–35.

19. Strom AR, Biggs RJ, Banigan EJ, Wang X, Chiu K, Herman C, et al. HP1α is a chromatin crosslinker that controls nuclear and mitotic chromosome mechanics. Elife. 2021 Jun 9;10:e63972.

20. Dos Santos Á, Cook AW, Gough RE, Schilling M, Olszok NA, Brown I, et al. DNA damage alters nuclear mechanics through chromatin reorganization. Nucleic Acids Res. 2021 Jan 11;49(1):340–53.

21. Deviri D, Safran SA. Balance of osmotic pressures determines the nuclear-to-cytoplasmic volume ratio of the cell. Proc Natl Acad Sci U S A. 2022 May 24;119(21):e2118301119.

22. Guilluy C, Osborne LD, Van Landeghem L, Sharek L, Superfine R, Garcia-Mata R, et al. Isolated nuclei adapt to force and reveal a mechanotransduction pathway within the nucleus. Nat Cell Biol. 2014 Apr;16(4):376–81.

23. Yue X, Cui J, Sun Z, Liu L, Li Y, Shao L, et al. Nuclear softening mediated by Sun2 suppression delays mechanical stress-induced cellular senescence. Cell Death Discov. 2023 May 17;9(1):167.

24. Kobiler O, Weitzman MD. Herpes simplex virus replication compartments: From naked release to recombining together. PLoS Pathog. 2019 Jun;15(6):e1007714.

25. Church GA, Dasgupta A, Wilson DW. Herpes simplex virus DNA packaging without measurable DNA synthesis. J Virol. 1998 Apr;72(4):2745–51.

26. Heming JD, Conway JF, Homa FL. Herpesvirus Capsid Assembly and DNA Packaging. Adv Anat Embryol Cell Biol. 2017;223:119–42.

27. Monier K, Armas JC, Etteldorf S, Ghazal P, Sullivan KF. Annexation of the interchromosomal space during viral infection. Nat Cell Biol. 2000 Sep;2(9):661–5.

28. Aho V, Mäntylä E, Ekman A, Hakanen S, Mattola S, Chen JH, et al. Quantitative Microscopy Reveals Stepwise Alteration of Chromatin Structure during Herpesvirus Infection. Viruses. 2019 Oct 11;11(10):935.

29. McSwiggen DT, Hansen AS, Teves SS, Marie-Nelly H, Hao Y, Heckert AB, et al. Evidence for DNA-mediated nuclear compartmentalization distinct from phase separation. Elife. 2019 May 7;8:e47098.

30. Seyffert M, Georgi F, Tobler K, Bourqui L, Anfossi M, Michaelsen K, et al. The HSV-1 Transcription Factor ICP4 Confers Liquid-Like Properties to Viral Replication Compartments. Int J Mol Sci. 2021 Apr 24;22(9):4447.

31. Caragliano E, Bonazza S, Frascaroli G, Tang J, Soh TK, Grünewald K, et al. Human cytomegalovirus forms phase-separated compartments at viral genomes to facilitate viral replication. Cell Rep. 2022 Mar 8;38(10):110469.

32. Aho V, Myllys M, Ruokolainen V, Hakanen S, Mäntylä E, Virtanen J, et al. Chromatin organization regulates viral egress dynamics. Sci Rep. 2017 Jun 16;7(1):3692.

957 33. Aho V, Salminen S, Mattola S, Gupta A, Flomm F, Sodeik B, et al. Infection-induced
958 chromatin modifications facilitate translocation of herpes simplex virus capsids to the
959 inner nuclear membrane. PLoS Pathog. 2021 Dec;17(12):e1010132.

960 34. Bosse JB, Hogue IB, Feric M, Thiberge SY, Sodeik B, Brangwynne CP, et al. Remodeling
961 nuclear architecture allows efficient transport of herpesvirus capsids by diffusion. Proc
962 Natl Acad Sci U S A. 2015 Oct 20;112(42):E5725-5733.

963 35. Lewis HC, Kelnhofer-Millevolte LE, Brinkley MR, Arbach HE, Arnold EA, Sanders S,
964 et al. HSV-1 exploits host heterochromatin for nuclear egress. J Cell Biol. 2023 Sep
965 4;222(9):e202304106.

966 36. González-Almela E, Castells-Garcia A, Le Dily F, Merino MF, Carnevali D, Cusco P, et
967 al. Herpes simplex virus type 1 reshapes host chromatin architecture via transcription
968 machinery hijacking. Nat Commun. 2025 Jun 19;16(1):5313.

969 37. Simpson-Holley M, Baines J, Roller R, Knipe DM. Herpes simplex virus 1 U(L)31 and
970 U(L)34 gene products promote the late maturation of viral replication compartments to
971 the nuclear periphery. J Virol. 2004 Jun;78(11):5591–600.

972 38. Bigalke JM, Heuser T, Nicastro D, Heldwein EE. Membrane deformation and scission by
973 the HSV-1 nuclear egress complex. Nat Commun. 2014 Jun 11;5:4131.

974 39. Bjerke SL, Roller RJ. Roles for herpes simplex virus type 1 UL34 and US3 proteins in
975 disrupting the nuclear lamina during herpes simplex virus type 1 egress. Virology. 2006
976 Apr 10;347(2):261–76.

977 40. Schäpe J, Prausse S, Radmacher M, Stick R. Influence of lamin A on the mechanical
978 properties of amphibian oocyte nuclei measured by atomic force microscopy. Biophys J.
979 2009 May 20;96(10):4319–25.

980 41. Hobson CM, Kern M, O'Brien ET, Stephens AD, Falvo MR, Superfine R. Correlating
981 nuclear morphology and external force with combined atomic force microscopy and light
982 sheet imaging separates roles of chromatin and lamin A/C in nuclear mechanics. Mol Biol
983 Cell. 2020 Jul 21;31(16):1788–801.

984 42. Hobson CM, Falvo MR, Superfine R. A survey of physical methods for studying nuclear
985 mechanics and mechanobiology. APL Bioeng. 2021 Dec;5(4):041508.

986 43. Kobiler O, Brodersen P, Taylor MP, Ludmir EB, Enquist LW. Herpesvirus replication
987 compartments originate with single incoming viral genomes. mBio. 2011;2(6):e00278-
988 11.

989 44. Chang L, Godinez WJ, Kim IH, Tektonidis M, de Lanerolle P, Eils R, et al. Herpesviral
990 replication compartments move and coalesce at nuclear speckles to enhance export of
991 viral late mRNA. Proc Natl Acad Sci U S A. 2011 May 24;108(21):E136-144.

992 45. Ou HD, Phan S, Deerinck TJ, Thor A, Ellisman MH, O'Shea CC. ChromEMT:
993 Visualizing 3D chromatin structure and compaction in interphase and mitotic cells.
994 Science. 2017 Jul 28;357(6349):eaag0025.

995 46. Jacob RJ, Morse LS, Roizman B. Anatomy of herpes simplex virus DNA. XII.
996 Accumulation of head-to-tail concatemers in nuclei of infected cells and their role in the
997 generation of the four isomeric arrangements of viral DNA. J Virol. 1979 Feb;29(2):448–
998 57.

999 47. Wang Y, Sherrard A, Zhao B, Melak M, Trautwein J, Kleinschnitz EM, et al. GPCR-
1000 induced calcium transients trigger nuclear actin assembly for chromatin dynamics. Nat
1001 Commun. 2019 Nov 21;10(1):5271.

1002 48. Goujon A, Colom A, Straková K, Mercier V, Mahecic D, Manley S, et al.
1003 Mechanosensitive Fluorescent Probes to Image Membrane Tension in Mitochondria,
1004 Endoplasmic Reticulum, and Lysosomes. J Am Chem Soc. 2019 Feb 27;141(8):3380–4.

1005 49. De Sandre-Giovannoli A, Bernard R, Cau P, Navarro C, Amiel J, Boccaccio I, et al. Lamin
1006 a truncation in Hutchinson-Gilford progeria. Science. 2003 Jun 27;300(5628):2055.

1007 50. Crisp M, Liu Q, Roux K, Rattner JB, Shanahan C, Burke B, et al. Coupling of the nucleus
1008 and cytoplasm: role of the LINC complex. J Cell Biol. 2006 Jan 2;172(1):41–53.

1009 51. Babatz TD, Spear ED, Xu W, Sun OL, Nie L, Carpenter EP, et al. Site specificity
1010 determinants for prelamin A cleavage by the zinc metalloprotease ZMPSTE24. J Biol
1011 Chem. 2021;296:100165.

1012 52. Fu B, Wang L, Li S, Dorf ME. ZMPSTE24 defends against influenza and other
1013 pathogenic viruses. J Exp Med. 2017 Apr 3;214(4):919–29.

1014 53. Stott-Marshall RJ, Foster TL. Inhibition of Arenavirus Entry and Replication by the Cell-
1015 Intrinsic Restriction Factor ZMPSTE24 Is Enhanced by IFITM Antiviral Activity. Front
1016 Microbiol. 2022;13:840885.

1017 54. Serrano JB, da Cruz E Silva OAB, Rebelo S. Lamina Associated Polypeptide 1 (LAP1)
1018 Interactome and Its Functional Features. Membranes (Basel). 2016 Jan 15;6(1):8.

1019 55. Luithle N, de Bos JU, Hovius R, Maslennikova D, Lewis RT, Ungricht R, et al. Torsin
1020 ATPases influence chromatin interaction of the Torsin regulator LAP1. Elife. 2020 Dec
1021 15;9:e63614.

1022 56. Wang N, Tytell JD, Ingber DE. Mechanotransduction at a distance: mechanically
1023 coupling the extracellular matrix with the nucleus. Nat Rev Mol Cell Biol. 2009
1024 Jan;10(1):75–82.

1025 57. Soh TK, Davies CTR, Muenzner J, Hunter LM, Barrow HG, Connor V, et al. Temporal
1026 Proteomic Analysis of Herpes Simplex Virus 1 Infection Reveals Cell-Surface
1027 Remodeling via pUL56-Mediated GOPC Degradation. Cell Rep. 2020 Oct
1028 6;33(1):108235.

1029 58. Procter DJ, Furey C, Garza-Gongora AG, Kosak ST, Walsh D. Cytoplasmic control of
1030 intranuclear polarity by human cytomegalovirus. Nature. 2020 Nov;587(7832):109–14.

1031 59. Itano N, Okamoto S ichi, Zhang D, Lipton SA, Ruoslahti E. Cell spreading controls
1032 endoplasmic and nuclear calcium: a physical gene regulation pathway from the cell
1033 surface to the nucleus. Proc Natl Acad Sci U S A. 2003 Apr 29;100(9):5181–6.

1034 60. Miyano T, Suzuki A, Konta H, Sakamoto N. Hyperosmotic Stress Promotes the Nuclear
1035 Translocation of TFEB in Tubular Epithelial Cells Depending on Intracellular Ca2+
1036 Signals via TRPML Channels. Cell Mol Bioeng. 2025 Feb;18(1):39–52.

1037 61. Phengchat R, Takata H, Morii K, Inada N, Murakoshi H, Uchiyama S, et al. Calcium ions
1038 function as a booster of chromosome condensation. Sci Rep. 2016 Dec 2;6:38281.

1039 62. Arsenovic PT, Ramachandran I, Bathula K, Zhu R, Narang JD, Noll NA, et al. Nesprin-
1040 2G, a Component of the Nuclear LINC Complex, Is Subject to Myosin-Dependent
1041 Tension. Biophys J. 2016 Jan 5;110(1):34–43.

1042 63. van der Linden FH, Mahlandt EK, Arts JJG, Beumer J, Puschhof J, de Man SMA, et al.
1043 A turquoise fluorescence lifetime-based biosensor for quantitative imaging of
1044 intracellular calcium. Nat Commun. 2021 Dec 9;12(1):7159.

1045 64. Linden FH van der, Thornquist SC, Beek RM ter, Huijts JY, Hink MA, Jr TWG, et al. A
1046 green lifetime biosensor for calcium that remains bright over its full dynamic range. eLife.
1047 2025 Jan 1;14.

1048 65. Evilevitch A, Hohlbauch SV. Intranuclear HSV-1 DNA ejection induces major
1049 mechanical transformations suggesting mechanoprotection of nucleus integrity. Proc Natl
1050 Acad Sci U S A. 2022 Mar 1;119(9):e2114121119.

1051 66. Ashby MF, Bréchet YJM. Designing hybrid materials. Acta Materialia. 2003 Nov
1052 25;51(19):5801–21.

1053 67. Kreger ST, Bell BJ, Bailey J, Stites E, Kuske J, Waisner B, et al. Polymerization and
1054 matrix physical properties as important design considerations for soluble collagen
1055 formulations. Biopolymers. 2010 Aug;93(8):690–707.

1056 68. Sarrigiannidis SO, Rey JM, Dobre O, González-García C, Dalby MJ, Salmeron-Sanchez
1057 M. A tough act to follow: collagen hydrogel modifications to improve mechanical and
1058 growth factor loading capabilities. Materials Today Bio. 2021 Mar 1;10:100098.

1059 69. Finan JD, Chalut KJ, Wax A, Guilak F. Nonlinear osmotic properties of the cell nucleus.
1060 Ann Biomed Eng. 2009 Mar;37(3):477–91.

1061 70. Zheng S, Li Y, Shao Y, Li L, Song F. Osmotic Pressure and Its Biological Implications.
1062 Int J Mol Sci. 2024 Mar 14;25(6):3310.

1063 71. Lammerding J, Fong LG, Ji JY, Reue K, Stewart CL, Young SG, et al. Lamins A and C
1064 but not lamin B1 regulate nuclear mechanics. J Biol Chem. 2006 Sep 1;281(35):25768–
1065 80.

1066 72. Neelam S, Chancellor TJ, Li Y, Nickerson JA, Roux KJ, Dickinson RB, et al. Direct force
1067 probe reveals the mechanics of nuclear homeostasis in the mammalian cell. Proc Natl
1068 Acad Sci U S A. 2015 May 5;112(18):5720–5.

1069 73. Broers JLV, Peeters EAG, Kuijpers HJH, Endert J, Bouten CVC, Oomens CWJ, et al.
1070 Decreased mechanical stiffness in LMNA-/- cells is caused by defective nucleo-
1071 cytoskeletal integrity: implications for the development of laminopathies. Hum Mol
1072 Genet. 2004 Nov 1;13(21):2567–80.

1073 74. Gruenbaum Y, Foisner R. Lamins: nuclear intermediate filament proteins with
1074 fundamental functions in nuclear mechanics and genome regulation. Annu Rev Biochem.
1075 2015;84:131–64.

1076 75. Reynolds AE, Liang L, Baines JD. Conformational changes in the nuclear lamina induced
1077 by herpes simplex virus type 1 require genes U(L)31 and U(L)34. J Virol. 2004
1078 Jun;78(11):5564–75.

1079 76. Mou F, Forest T, Baines JD. US3 of herpes simplex virus type 1 encodes a promiscuous
1080 protein kinase that phosphorylates and alters localization of lamin A/C in infected cells. J
1081 Virol. 2007 Jun;81(12):6459–70.

1082 77. Takeshima K, Maruzuru Y, Koyanagi N, Kato A, Kawaguchi Y. Redundant and Specific
1083 Roles of A-Type Lamins and Lamin B Receptor in Herpes Simplex Virus 1 Infection. J
1084 Virol. 2022 Dec 21;96(24):e0142922.

1085 78. Leach NR, Roller RJ. Significance of host cell kinases in herpes simplex virus type 1
1086 egress and lamin-associated protein disassembly from the nuclear lamina. Virology. 2010
1087 Oct 10;406(1):127–37.

1088 79. Enyedi B, Jelcic M, Niethammer P. The Cell Nucleus Serves as a Mechanotransducer of
1089 Tissue Damage-Induced Inflammation. Cell. 2016 May 19;165(5):1160–70.

1090 80. Thorsen MK, Lai A, Lee MW, Hoogerheide DP, Wong GCL, Freed JH, et al. Highly
1091 Basic Clusters in the Herpes Simplex Virus 1 Nuclear Egress Complex Drive Membrane
1092 Budding by Inducing Lipid Ordering. mBio. 2021 Aug 31;12(4):e0154821.

1093 81. Jiao S, Li C, Guo F, Zhang J, Zhang H, Cao Z, et al. SUN1/2 controls macrophage
1094 polarization via modulating nuclear size and stiffness. Nat Commun. 2023 Oct
1095 12;14(1):6416.

1096 82. Krshnan L, Siu WS, Van de Weijer M, Hayward D, Guerrero EN, Gruneberg U, et al.
1097 Regulated degradation of the inner nuclear membrane protein SUN2 maintains nuclear
1098 envelope architecture and function. Elife. 2022 Nov 1;11:e81573.

1099 83. Jiao S, Li C, Guo F, Zhang J, Zhang H, Cao Z, et al. SUN1/2 controls macrophage
1100 polarization via modulating nuclear size and stiffness. Nat Commun. 2023 Oct
1101 12;14(1):6416.

1102 84. Xiang Y, Zheng K, Ju H, Wang S, Pei Y, Ding W, et al. Cofilin 1-mediated biphasic F-
1103 actin dynamics of neuronal cells affect herpes simplex virus 1 infection and replication. J
1104 Virol. 2012 Aug;86(16):8440–51.

1105 85. Mih JD, Marinkovic A, Liu F, Sharif AS, Tschumperlin DJ. Matrix stiffness reverses the
1106 effect of actomyosin tension on cell proliferation. J Cell Sci. 2012 Dec 15;125(Pt
1107 24):5974–83.

1108 86. Gilbert HTJ, Mallikarjun V, Dobre O, Jackson MR, Pedley R, Gilmore AP, et al. Nuclear
1109 decoupling is part of a rapid protein-level cellular response to high-intensity mechanical
1110 loading. Nat Commun. 2019 Sep 12;10(1):4149.

1111 87. Cruz-Palomar K, Hawkins J, Vandal C, Quenneville J, Gagnon É, Lippé R. SUN2
1112 Modulates the Propagation of HSV-1. J Virol. 2022 May 11;96(9):e0045322.

1113 88. Rosencrance CD, Walsh D. Microtubule mechanotransduction refines cytomegalovirus
1114 interactions with and remodeling of host chromatin. Nat Commun. 2025 Aug
1115 13;16(1):7507.

1116 89. Wild P, Senn C, Manera CL, Sutter E, Schraner EM, Tobler K, et al. Exploring the nuclear
1117 envelope of herpes simplex virus 1-infected cells by high-resolution microscopy. J Virol.
1118 2009 Jan;83(1):408–19.

1119 90. Datta S, Snow CJ, Paschal BM. A pathway linking oxidative stress and the Ran GTPase
1120 system in progeria. Mol Biol Cell. 2014 Apr;25(8):1202–15.

1121 91. Danielsson BE, Peters HC, Bathula K, Spear LM, Noll NA, Dahl KN, et al. Progerin-
1122 expressing endothelial cells are unable to adapt to shear stress. Biophys J. 2022 Feb
1123 15;121(4):620–8.

1124 92. Everett RD, Sourvinos G, Orr A. Recruitment of herpes simplex virus type 1
1125 transcriptional regulatory protein ICP4 into foci juxtaposed to ND10 in live, infected
1126 cells. J Virol. 2003 Mar;77(6):3680–9.

1127 93. Sandbaumhüter M, Döhner K, Schipke J, Binz A, Pohlmann A, Sodeik B, et al. Cytosolic
1128 herpes simplex virus capsids not only require binding inner tegument protein pUL36 but
1129 also pUL37 for active transport prior to secondary envelopment. Cell Microbiol. 2013
1130 Feb;15(2):248–69.

1131 94. Ivanova L, Buch A, Döhner K, Pohlmann A, Binz A, Prank U, et al. Conserved
1132 Tryptophan Motifs in the Large Tegument Protein pUL36 Are Required for Efficient
1133 Secondary Envelopment of Herpes Simplex Virus Capsids. J Virol. 2016 Jun
1134 1;90(11):5368–83.

1135 95. Buch A, Müller O, Ivanova L, Döhner K, Bialy D, Bosse JB, et al. Inner tegument proteins
1136 of Herpes Simplex Virus are sufficient for intracellular capsid motility in neurons but not
1137 for axonal targeting. PLoS Pathog. 2017 Dec;13(12):e1006813.

1138 96. Loconte V, Chen JH, Cortese M, Ekman A, Le Gros MA, Larabell C, et al. Using soft X-
1139 ray tomography for rapid whole-cell quantitative imaging of SARS-CoV-2-infected cells.
1140 Cell Rep Methods. 2021 Nov 22;1(7):100117.

1141 97. Chen JH, Vanslembrouck B, Loconte V, Ekman A, Cortese M, Bartenschlager R, et al. A
1142 protocol for full-rotation soft X-ray tomography of single cells. STAR Protoc. 2022 Mar
1143 18;3(1):101176.

1144 98. Parkinson DY, Knoechel C, Yang C, Larabell CA, Le Gros MA. Automatic alignment
1145 and reconstruction of images for soft X-ray tomography. J Struct Biol. 2012
1146 Feb;177(2):259–66.

1147 99. Leclerc S, Gupta A, Ruokolainen V, Chen JH, Kunnas K, Ekman AA, et al. Progression
1148 of herpesvirus infection remodels mitochondrial organization and metabolism. PLoS
1149 Pathog. 2024 Apr;20(4):e1011829.

100. Belevich I, Joensuu M, Kumar D, Vihinen H, Jokitalo E. Microscopy Image Browser: A Platform for Segmentation and Analysis of Multidimensional Datasets. PLoS Biol. 2016 Jan;14(1):e1002340.

101. Li CH, Lee CK. Minimum cross entropy thresholding. Pattern Recognition. 1993 Apr 1;26(4):617–25.

102. Kaikkonen MU, Niskanen H, Romanoski CE, Kansanen E, Kivelä AM, Laitalainen J, et al. Control of VEGF-A transcriptional programs by pausing and genomic compartmentalization. Nucleic Acids Res. 2014 Nov 10;42(20):12570–84.

103. Langmead B, Trapnell C, Pop M, Salzberg SL. Ultrafast and memory-efficient alignment of short DNA sequences to the human genome. Genome Biol. 2009;10(3):R25.

104. Ahrens JP, Geveci B, Law C. ParaView: An end-user tool for large-data visualization. In: Visualization Handbook. Elsevier; 2005. p. 717–31.

Supporting Information

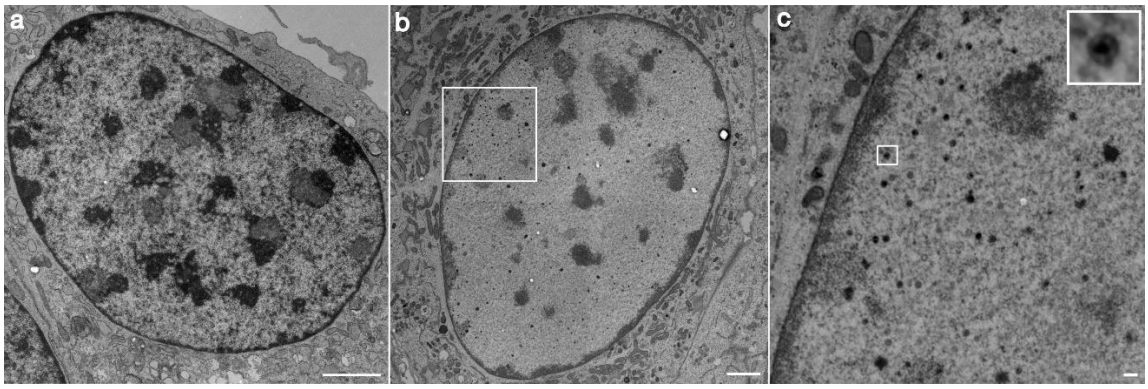

S1 Fig. Distribution of nuclear chromatin and viral DNA in full capsids. Representative transmission electron microscopy images of **(A)** a noninfected and **(B)** an infected MEF cell at 8 hpi. ChromEM labeling was used to enhance DNA contrast. **(C)** Full viral capsids with DNA staining are shown. White squares show the magnified nucleoplasm and a full capsid. Scale bars, 2 µm (A, B) and 0.2 µm (C).

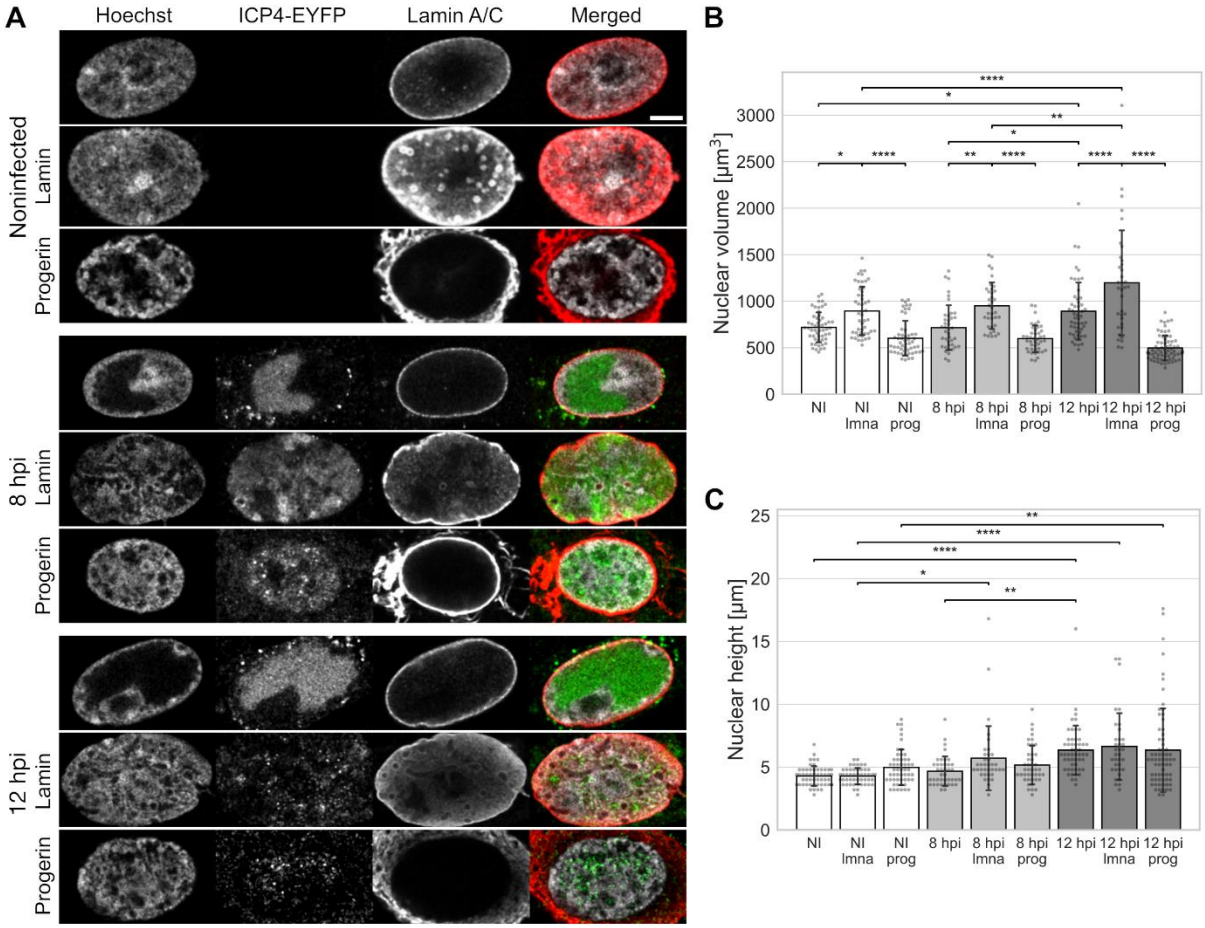

S2 Fig. Overexpression of lamin A enhances nuclear growth. (A) Representative confocal images of noninfected and HSV-1 EYFP-ICP4-infected Vero cells at 8 and 12 hpi together with Vero cells overexpressing lamin A (lmna) and expressing progerin (prog). Lamin A/C was labeled with lamin A/C antibody (red), EYFP-ICP4 (green) shows the localization of the VRC, and the chromatin was labeled with Hoechst 33342 (grey). Quantitative analysis of **(B)** the volume and **(C)** the height of the nucleus in noninfected (NI) and infected cells (n=53, 48, 53, 40, 36, 42, 52, 35, and 67 for the bars from left to right). The error bars show the standard deviation. Statistical significance was determined using Tukey's test, and the significance values are denoted as **** ($p < 0.0001$), ** ($p < 0.01$), or * ($p < 0.05$). Only values of the same time point or treatment were statistically compared. Nonsignificant differences ($p \geq 0.05$) are not labeled.

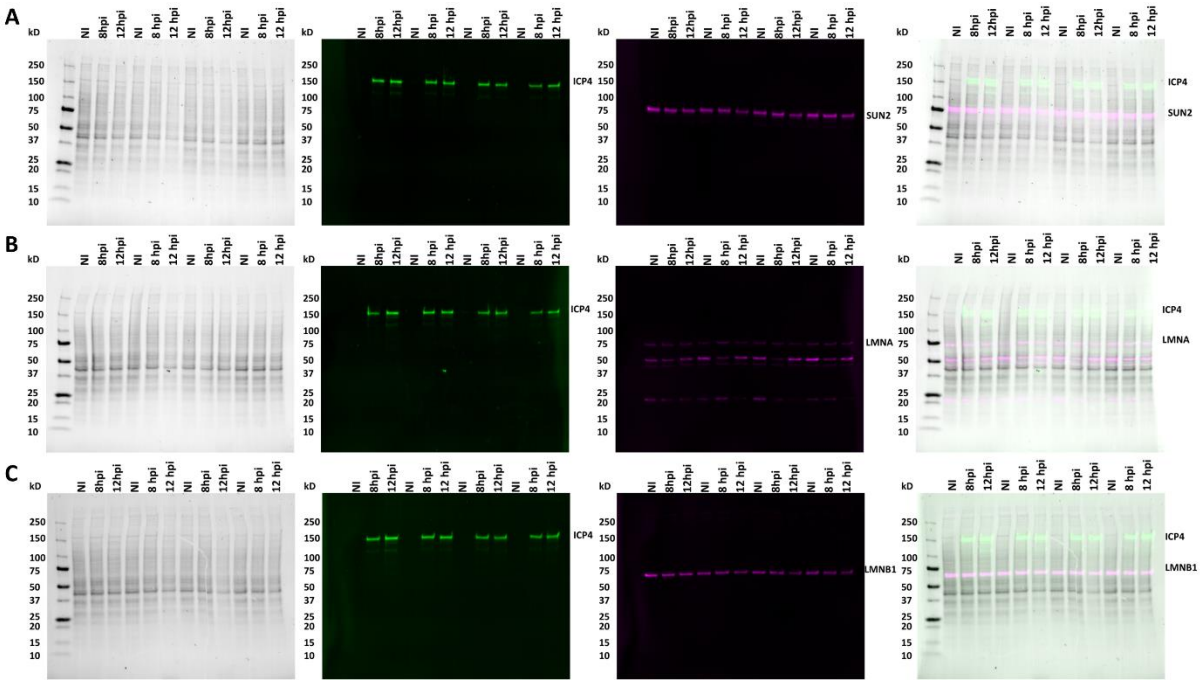

S3 Fig. Expression of SUN2, lamin A, and lamin B. Western blot of noninfected and infected (8 and 12 hpi) Vero cell lysates were analyzed for total protein and SUN2 **(A)**, LMNA **(B)**, or LMNB1 **(C)**. An antibody against ICP4 was used as a marker for viral infection. Each set of noninfected and infected lysates represents a replicate experiment (n = 4).

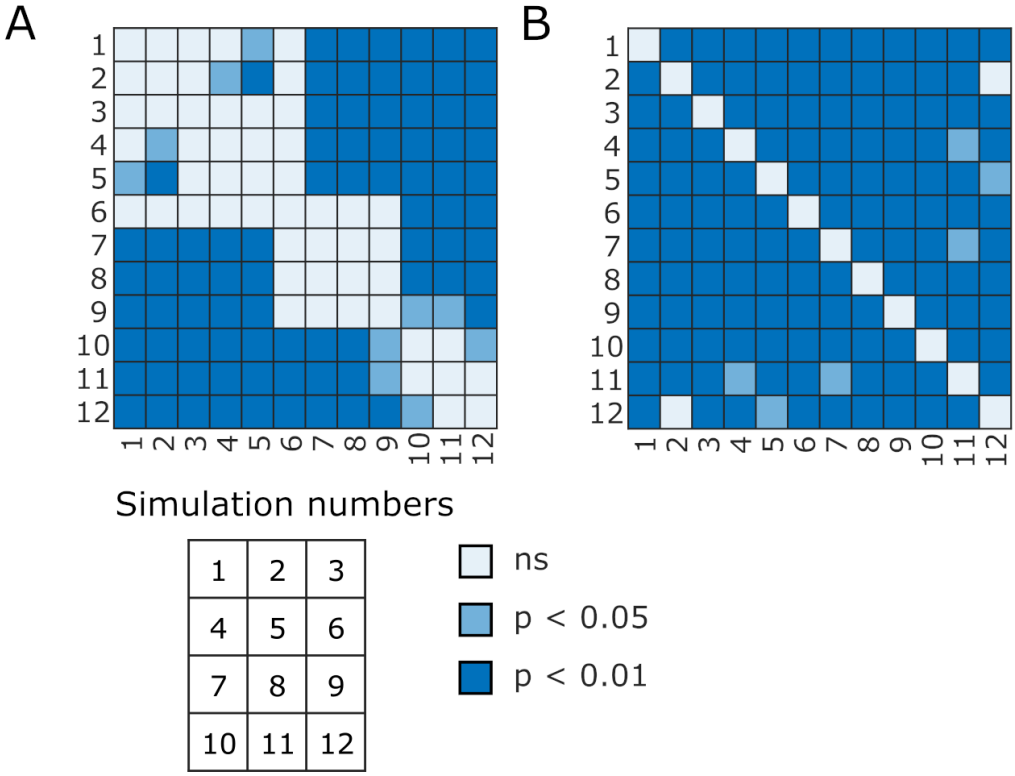

S4 Fig. Statistical significances between simulations. Simulation case numbers and statistical significances between simulations presented in Figure 6 for **(A)** Young's moduli (6F) and **(B)** nuclear envelope membrane tension (6G). Statistical significances were determined using the Games-Howell test. The significance values are denoted as $p<0.01$, $p<0.05$, or ns (not significant).

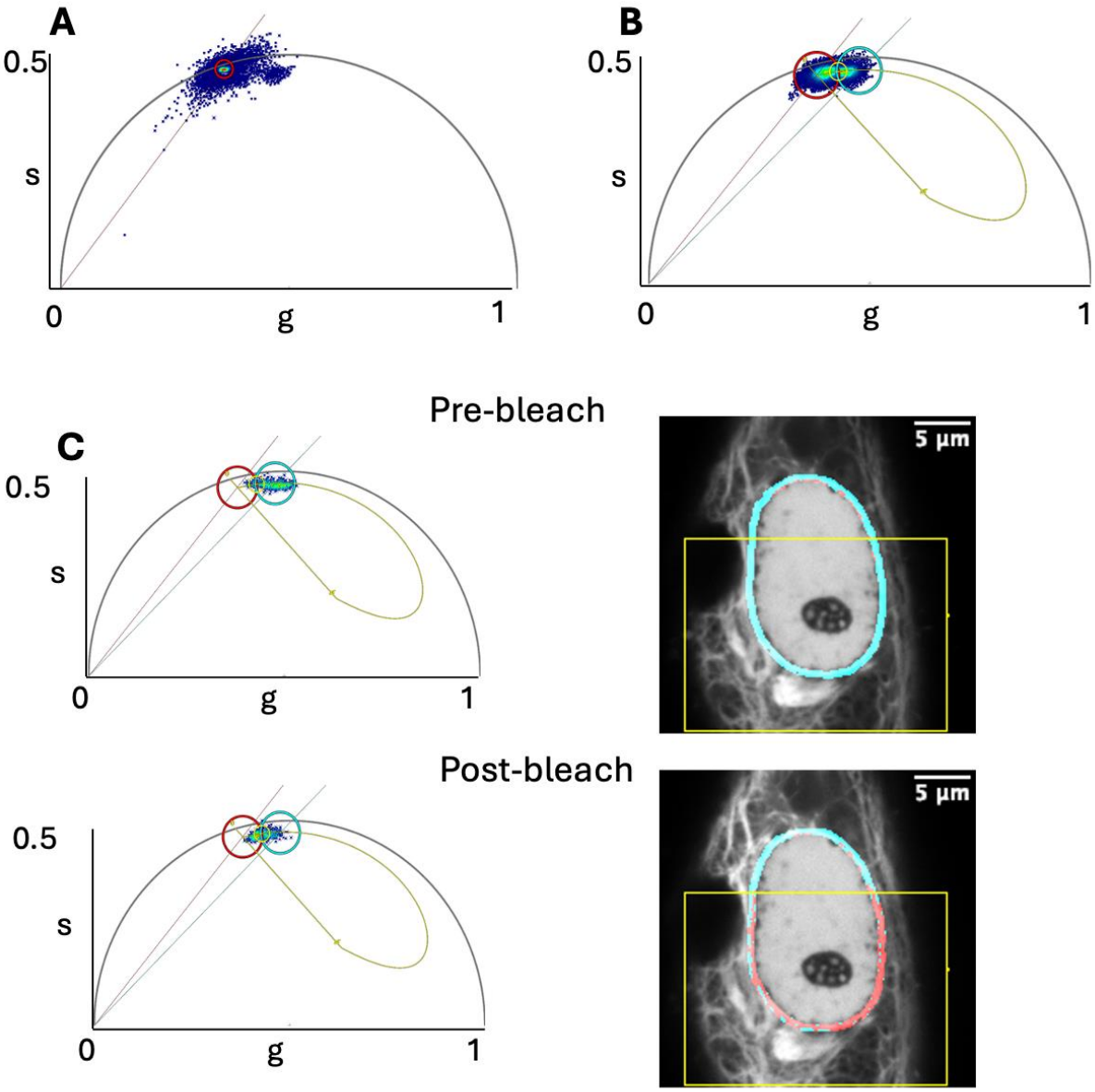

1213

1214 **S5 Fig. Tension sensor analysis of the mechanical forces transmitted to the nucleus.** (**A**)
1215 Phasor plot analysis of the Nesprin TS donor fluorophore mTFP1 measured in noninfected and
1216 infected cells shows a lifetime distribution from 2.65ns to 2.71ns. (**B**) Phasor distribution of
1217 mTFP1 from FLIM measurement of noninfected and infected cells. The FRET trajectory was
1218 generated using LAS X (4.5.0) phasor analysis tool by setting the donor-only lifetime to 2.71
1219 ns based on mTFP1 measurements, by locating the autofluorescence from non-transfected
1220 cells, and by adjusting the background contribution to ensure the trajectory passes through the
1221 measured phasor clouds. The division between low FRET/high tension (red phasor cursor at

1222 2.47ns) and high FRET/low tension (cyan phasor cursor at 2.01ns) was set to 10% FRET
1223 efficiency (yellow phasor cursor). The pixels at the nuclear envelope (NE) of the measured
1224 cells were divided into low or high FRET areas according to their lifetime distribution in the
1225 phasor plot, and their relative amount was quantified. (**C**) An acceptor bleaching experiment to
1226 validate the Nesprin TS working in our system. FRET at the NE decreases after bleaching the
1227 acceptor from the area shown by the yellow box in a living cell.

1228

1229

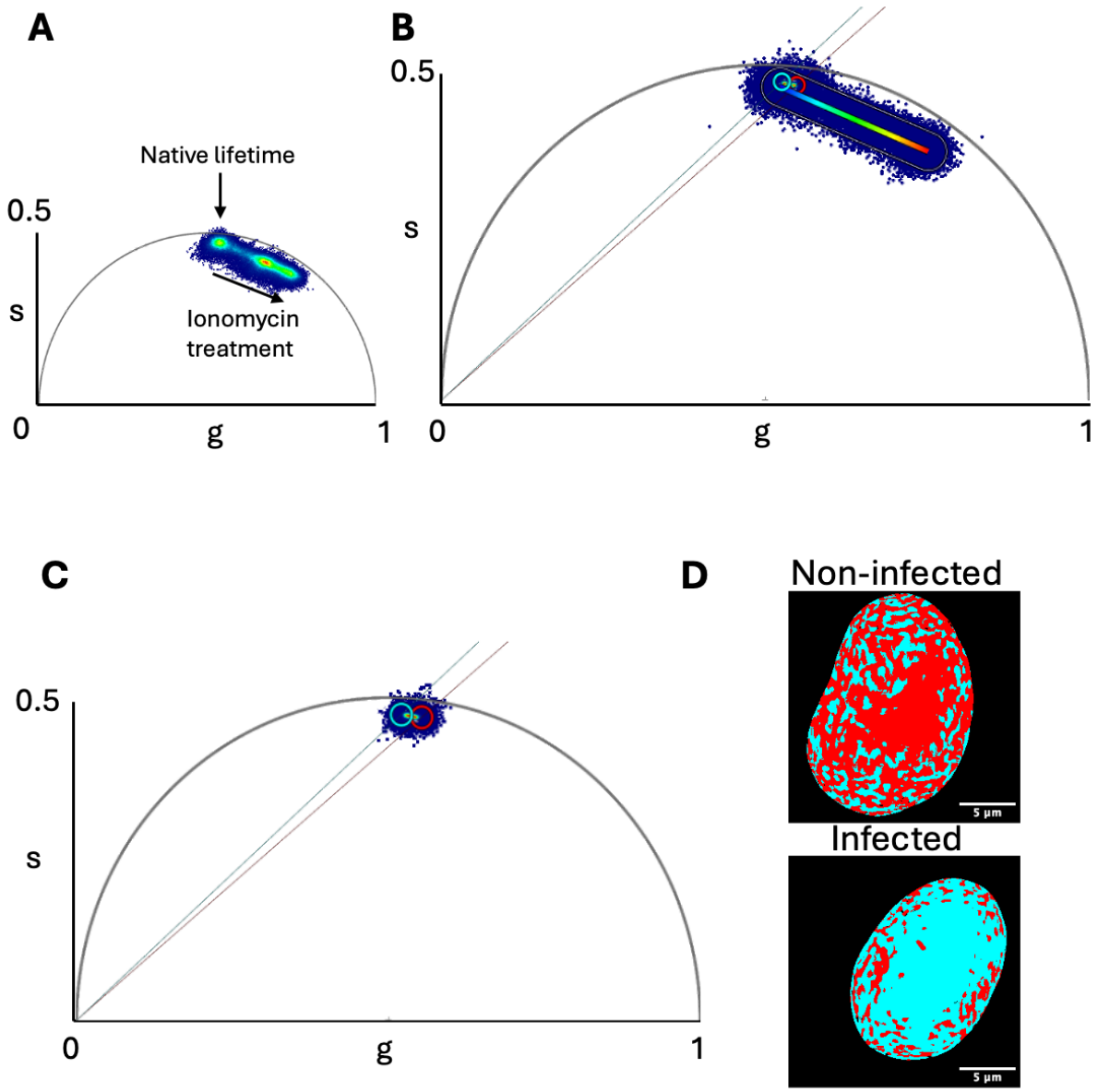

1230

1231 **S6 Fig. Detection of nuclear Ca^{2+} concentration using G-Ca-FLITS biosensor. (A)** Phasor
1232 plot of the phasor distribution of live FLIM imaging of 3xnls-G-Ca-FLITS transfected cells.
1233 The phasor cloud in native cell state starts approximately from s=0.5, g=0.5 (top-center) and
1234 moves diagonally towards down-right during ionomycin treatment, confirming the expected
1235 shorter lifetime in high calcium concentration. **(B)** The calibration line (rainbow), generated
1236 according to the ionomycin measurement, demonstrated longer lifetime (cyan cursor) in
1237 infected cells than in noninfected cells (red cursor). This indicated reduced calcium
1238 concentration in infected cells. (**C**) Phasor distribution of noninfected and infected nuclei

1239 lifetime, and their division between low calcium (longer lifetime cyan phasor cursor set to 3.71
1240 ns) and high calcium (shorter lifetime red phasor cursor set to 3.46 ns). (**D**) The pseudo-colored
1241 spatial distribution of pixels with high and low calcium concentration according to their
1242 lifetime distribution in the phasor plot in representative non-infected and 8 hpi nuclei.
1243
1244
1245
1246
1247 **S1 Movie. AFM analysis of nuclear stiffness.** Animation of AFM imaging of infected Vero
1248 cells at 4 hpi (left). Retraction curves of four measurements showing the force (deflection)
1249 versus cell height in living cells, retraction (cyan) and extension (blue) curves, and contact
1250 points (arrows) are shown (right). The vertical red line shows the progression of the
1251 measurement.
1252
1253 **S2 Movie. Infection-induced changes of the nucleus.** Animation of cryo-soft X-ray (SXT)
1254 tomography imaging data of noninfected (NI) and infected MEF cells at 8 hpi. The high- (blue)
1255 and low-density chromatin (yellow), as well as the viral replication compartment (VRC, green),
1256 are shown.
1257
1258 **S3 Movie. Chromatin organization in the nuclear periphery is altered in infection.**
1259 Animation of focused ion-beam scanning electron microscopy (FIB-SEM) imaging data of
1260 noninfected and infected MEF cells at 8 hpi. The color bar indicates high and low chromatin
1261 thickness (yellow-blue). The nuclear envelope (cyan) and viral capsids (grey) are shown.
1262

1263 **S4 Movie. Remodeling of nuclear organization during the growth of the viral replication**
1264 **compartment.** Expansion of VRC as the infection proceeds. The chromatin is shown in blue,
1265 VRC in green, lamina-associated domains (LADs) of the chromatin and chromatin crosslinks
1266 in cyan, and the NE in grey.
1267
1268 **S5 Movie. Simulated AFM measurement of the infected cell.** AFM measurement of the
1269 nuclear stiffness of an infected cell. The effect of the colloidal probe of the cantilever (white)
1270 over the nucleus is presented. The cell membrane and cytoplasm are not presented. The
1271 chromatin is shown in blue, the lamina-associated domains (LADs) of the chromatin and
1272 chromatin crosslinks in green, and the NE in grey. The VRC located in the central region of
1273 the nucleus is not shown.
1274
1275 **S1 Table. Transcription of nuclear lamins and lamin-associated proteins is regulated in**
1276 **response to viral infection.** The table presents the results of GRO-seq analysis showing
1277 upregulated (green-blue) or downregulated (red-orange) lamins and lamin-associated protein
1278 genes in infected Vero cells at 4 and 8 hpi.
1279
1280 **S1 Text. Description of the model and the parameters**. A detailed description of the model
1281 assumptions, equations, solution method, atomic force microscopy simulations and analysis,
1282 the fitting process, and the parameter values.